AD-A165 692 SOLID STATE RESEARCH(U) MASSACHUSETTS INST OF TECH 1/1
LEXINGTON LINCOLN LAB A L MCWHORTER 15 MAY 85 1985:2
ESD-TR-85-214 F19628-85-C-0002

UNCLASSIFIED F/G 20/2 NL

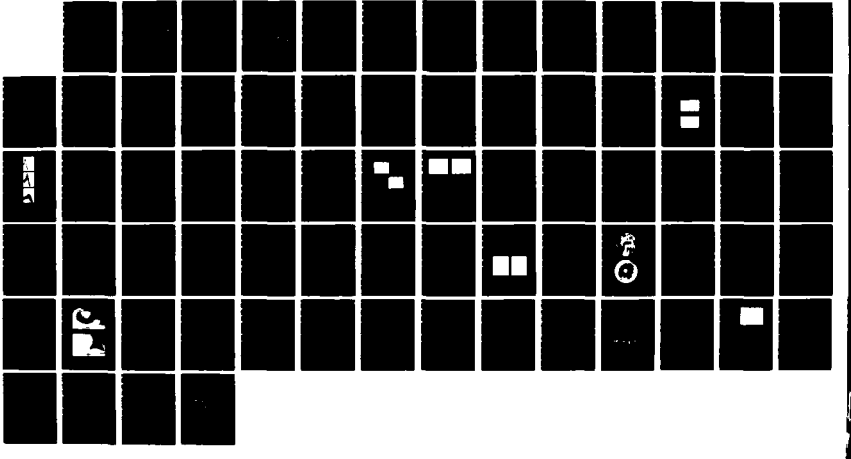

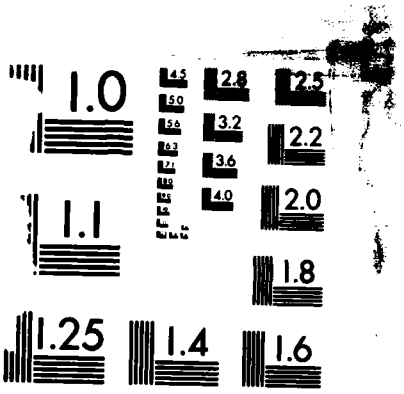

(2)

ESD-TR-85-214

AD-A165 692

Quarterly Technical Report

Solid State Research

1985:2

Lincoln Laboratory

MASSACHUSETTS INSTITUTE OF TECHNOLOGY

LEXINGTON, MASSACHUSETTS

Prepared under Electronic Systems Division Contract F19628-85-C-0002.

The work reported in this document was performed at Lincoln Laboratory, a center for research operated by Massachusetts Institute of Technology, with the support of the Department of the Air Force under Contract F19628-85-C-0002.

The views and conclusions contained in this document are those of the contractor and should not be interpreted as necessarily representing the official policies, either expressed or implied, of the United States Government.

The ESD Public Affairs Office has reviewed this report, and it is releasable to the National Technical Information Service, where it will be available to the general public, including foreign nationals.

This technical report has been reviewed and is approved for publication.

FOR THE COMMANDER

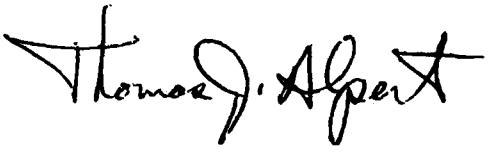

Thomas J. Alpert, Major, USAF
Chief, ESD Lincoln Laboratory Project Office

Non-Lincoln Recipients

PLEASE DO NOT RETURN

Permission is given to destroy this document *when it is no longer needed.*

MASSACHUSETTS INSTITUTE OF TECHNOLOGY
LINCOLN LABORATORY

SOLID STATE RESEARCH

QUARTERLY TECHNICAL REPORT

1 FEBRUARY — 30 APRIL 1985

ISSUED 31 OCTOBER 1985

LEXINGTON MASSACHUSETTS

ABSTRACT

This report covers in detail the solid state research work of the Solid State Division at Lincoln Laboratory for the period 1 February through 30 April 1985. The topics covered are Solid State Device Research, Quantum Electronics, Materials Research, Microelectronics, and Analog Device Technology. Funding is primarily provided by the Air Force, with additional support provided by the Army, DARPA, Navy, NASA, and DOE.

TABLE OF CONTENTS

LIST OF ILLUSTRATIONS

INTRODUCTION

1. SOLID STATE DEVICE RESEARCH

Integrated-optical components are being developed for fiber gyroscope systems. A double-Y waveguide branch circuit with an insertion loss of only 6 dB has been fabricated in $LiNbO_3$. Serrodyne optical frequency translation with 40 dB sideband suppression has been achieved using a $LiNbO_3$ phase modulator.

The small-signal frequency response of short-cavity mass-transported buried heterostructure lasers with minimal parasitic contact pad capacitance has been measured. Initial results show that the highest relaxation frequency of 5 GHz is obtained in long lasers with high optical power.

2. QUANTUM ELECTRONICS

RC-limited response times of less than 100 ps have been attained for Au:InP Schottky barrier internal-photoemission detectors at a wavelength of 1.06 μm. The quantum efficiency of these detectors was enhanced by the use of gratings to couple incident optical energy into surface plasma waves that propagate along the Au film.

3. MATERIALS RESEARCH

Room-temperature operation has been achieved in GaAs/AlGaAs heterostructure diode lasers fabricated on a monolithic GaAs/Si substrate. These devices, which incorporate a large optical cavity structure grown by molecular beam epitaxy directly on a Si wafer, have exhibited threshold currents as low as 775 mA and power outputs as high as 27 mW/facet in pulsed operation.

The optical transmission of the intermediate Ge layer in the proposed GaAs/Ge/Si and $Ga_{0.72}Al_{0.28}As$/Ge/Si tandem solar cell structures has been calculated on the assumption that this layer has the optical properties reported for bulk Ge single crystals. The results show that the Ge layer must be extremely thin in order to avoid significant reduction in conversion efficiency due to optical losses. Even for a Ge layer only 0.15 μm thick, the efficiency would be reduced by at least 25% for the GaAs/Ge/Si structure and by at least 40% for the $Ga_{0.72}Al_{0.28}As$/Ge/Si structure.

4. MICROELECTRONICS

Permeable base transistors with a gain of 18.5 dB at 18 GHz have been fabricated using organometallic chemical vapor deposition (OMCVD). The extrapolated f_{max} exceeds the best previous result of approximately 100 GHz. Secondary ion mass spectrometry (SIMS) analysis shows that there is a large concentration of undesired impurities in the grating region of these devices. Improved performance is anticipated for future devices if these impurities can be eliminated.

Room temperature negative resistance and the resulting oscillations up to 20 GHz have been observed in double-barrier resonant tunneling structures.

Reduction in the number of subboundary defects has been achieved in silicon films produced by zone-melting recrystallization (ZMR). The defect density was reduced to approximately 10^6 by cm^{-2} by increasing both the thickness of the ZMR film and the underlying oxide layer.

A versatile dry etching process using a CCl_2F_2 plasma with small additions of O_2 or N_2 has been developed for GaAs which features etch rates of several microns a minute. This process combined with electroless plating of Pd has been used for ground-source connections in GaAs FETs.

5. ANALOG DEVICE TECHNOLOGY

A stripline gap-coupled resonator has been used to evaluate losses in thin films of different superconductors such as Nb, NbN, and Nb_3Sn between 200 MHz and 18 GHz at temperatures from 4.2 K to 25 K. These measurements indicate that NbN is a suitable material for superconductive signal-processing devices operating at 10 K.

Superconductive chirp filters with a 2.6-GHz bandwidth and dispersion times of up to 75 ns have been produced by stacking niobium-on-silicon stripline circuits assembled with a phenolic resin. A flat-weighted expander and Hamming-weighted compressor have exhibited relative sidelobe levels of −22 dB in pulse-compression tests, approaching those of shorter unstacked stripline circuits. Packaging refinements are expected to lead to sidelobe levels below −30 dB.

A method that has particular application to scattering measurements has been developed for the adaptive cancellation of the slowly varying portion of the response from a linear time-varying system. An estimate of the system's impulse response is obtained by matched filtering the outputs generated by wideband inputs. This estimated impulse response then is used to generate an estimate of subsequent system outputs that are subtracted from the actual output to yield only the rapidly time-varying portion of the system's output.

REPORTS ON SOLID STATE RESEARCH

1 February through 30 April 1985

PUBLISHED REPORTS

Journal Articles

JA No.			
5594	Surface Acoustic Wave Devices	D.E. Oates	Chapter 8 in *VLSI Electronics: Microstructure Science*, Vol. 9, N. Einspruch, Ed., (Academic Press, New York, 1985)
5596	Laser-Induced Chemistry for Microelectronics	R.M. Osgood T.F. Deutsch	Science **227**, 709 (1985)
5610	Submicrometer Patterning by Projected Excimer-Laser-Beam Induced Chemistry	D.J. Ehrlich J.Y. Tsao C.O. Bozler	J. Vac. Sci. Technol. B **3**, 1 (1985)
5662	Frequency Tuning Characteristics of a Q-Switched Co:MgF_2 Laser	S. Lovold* P.F. Moulton D.K. Killinger N. Menyuk	IEEE J. Quantum Electron. **QE-21**, 202 (1985)
5671	Selective Tungsten Silicide Formation by Ion-Beam Mixing and Rapid Thermal Annealing	B-Y. Tsaur C.K. Chen C.H. Anderson, Jr. D.L. Kwong*	J. Appl. Phys. **57**, 1890 (1985)
5680	UV-Laser Photodeposition of Patterned Catalyst Films from Adsorbate Mixtures	D.J. Ehrlich J.Y. Tsao*	Appl. Phys. Lett. **46**, 198 (1985)
5699	High-Power Second Harmonic Emission and Frequency Locking in a 28-GHz Gyrotron	B.G. Danly* W.J. Mulligan* R.J. Temkin* T.C.L.G. Sollner	Appl. Phys. Lett. **46**, 728 (1985)

* Author not at Lincoln Laboratory.

JA No.

5701	Planar GaAs *p-i-n* Photodiode with Picosecond Time Response	W. Lenth A. Chu L.J. Mahoney R.W. McClelland R.W. Mountain D.J. Silversmith	Appl. Phys. Lett. **46**, 191 (1985)
5703	A Novel GaInAsP/InP Distributed Feedback Laser	Z-L. Liau D.C. Flanders J.N. Walpole N.L. DeMeo	Appl. Phys. Lett. **46**, 221 (1985)
5710	A Gallium Arsenide Overlapping Gate Charge-Coupled Device	K.B. Nichols B.E. Burke	IEEE Electron. Device Lett. **EDL-6**, 237 (1985)
5722	Wide-Bandwidth Guided-Wave Electro-optic Intensity Modulator at $\lambda = 3.39\ \mu m$	R.A. Becker R.H. Rediker T.A. Lind	Appl. Phys. Lett. **46**, 809 (1985)

Meeting Speeches

MS No.

6613	Low Power Ion-Beam-Assisted Etching of Indium Phosphide	N.L. DeMeo J.P. Donnelly F.J. O'Donnell M.W. Geis K.J. O'Connor	Nucl. Instrum. Methods **B7/8**, 814 (1985)
6642	Superconductive Convolver with Junction Ring Mixers	S.A. Reible	IEEE Trans. Magn. **MAG-21**, 193 (1985)
6674	Monolithic Integration of GaAs and Si	J.C.C. Fan	Extended Abstracts of the Sixteenth International Conference on Solid State Devices and Materials, Kobe, Japan, 30 August-1 September 1984, p. 115
6702	Wide-Band SAW/FET Programmable Transversal Filter	D.E. Oates D.L. Smythe J.B. Green R.W. Ralston A.C. Anderson	*1984 Ultrasonics Symposium Proceedings* (IEEE, New York, 1984), p. 312

MS No.			
6708	Application of SAW Convolvers to Spread-Spectrum Communication	J.H. Cafarella	*1984 Ultrasonics Symposium Proceedings* (IEEE, New York, 1984), p. 121
6709	Holographic-Grating Acoustic Devices	P.G. Gottschalk D.E. Oates P.V. Wright	*1984 Ultrasonics Symposium Proceedings* (IEEE, New York 1984), p. 97
6711	Superconductive Delay-Line Technology and Applications	R.S. Withers A.C. Anderson J.B. Green S.A. Reible	IEEE Trans. Magn. **MAG-21**, 186 (1985)
6712	Wideband Radar Signal Processor Based on SAW Convolvers	I. Yao E.M. Hauser C.A. Bouman G.T. Flynn J.H. Cafarella	*1984 Ultrasonics Symposium Proceedings* (IEEE, New York, 1984), p. 132
6731	Merged CMOS/Bipolar Technologies and Microwave MESFETS Utilizing Zone-Melting-Recrystallized SOI Films	B-Y. Tsaur H.K. Choi C.K. Chen C.L. Chen R.W. Mountain J.C.C. Fan	Proc. IEEE International Electron Devices Meeting, San Francisco, California, 9-12 December 1984, p. 812
6735	Signal Processing: Opportunities for Superconductive Circuits	R.W. Ralston	IEEE Trans. Magn. **MAG-21**, 181 (1985)

* * * * *

UNPUBLISHED REPORTS

Journal Articles

JA No.			
5672	Single-Mode Optical Waveguides and Phase Modulators in the InP Material System	J.P. Donnelly N.L. DeMeo F.J. Leonberger S.H. Groves P. Vohl F.J. O'Donnell	Accepted by IEEE J. Quantum Electron.

JA No.			
5709	Multigigahertz Lumped-Element Electrooptic Modulators	R.A. Becker	Accepted by IEEE J. Quantum Electron.
5715	Design Considerations for Flat-Plate Photovoltaic/Thermal Collectors	C.H. Cox, III P. Raghuraman	Accepted by Sol. Energy
5720	Enhanced Quantum Efficiency Internal Photoemission Detectors by Grating Coupling to Surface Plasma Waves	S.R.J. Brueck V. Diadiuk T. Jones W. Lenth*	Accepted by Appl. Phys. Lett.
5731	Persistent Photoconductivity in Quantum Well Resonators	T.C.L.G. Sollner H.Q. Le C.A. Correa W.D. Goodhue	Accepted by Appl. Phys. Lett.
5741	Fundamental Spectral Width of Laser Light	A. Mooradian	Accepted by Phys. Today

Meeting Speeches†

MS No.			
6647A	14-GHz Operation of Q-Switched Diode Lasers	D.Z. Tsang J.N. Walpole S.H. Groves Z-L. Liau	SPIE Technical Symposium East '85, Arlington, Virginia, 8-12 April 1985
6803	Integrated Optics Wavefront Measurement Sensor	R.H. Rediker T.A. Lind	
6818	High-Speed Lateral Photoconductors on Semi-insulating InGaAs and InP	V. Diadiuk S.H. Groves	
6879	Use of Spatial Time-Division Repetition Rate Multiplication of Mode-Locked Laser Pulses to Generate Microwave Radiation from Optoelectronic Switches	A. Mooradian	

† Titles of Meeting Speeches are listed for information only. No copies are available for distribution.

MS No.			
6891	Basic Concepts for the Design of High-Efficiency Single-Junction and Multibandgap Solar Cells	J.C.C. Fan	SPIE Technical Symposium East 85, Arlington, Virginia, 8-12 April 1985
6674B	Monolithic Integration of GaAs and Si	J.C.C. Fan	Seminar, Ford Motor Company, Dearborn, Michigan, 7 February 1985
6674C	Monolithic Integration of GaAs and Si	J.C.C. Fan	Seminar, Dept. of Electrical Engineering and Computer Sciences, University of California, Berkeley, California, 13 February 1985
6713B	Beam-Assisted Chemistry	D.J. Ehrlich	American Chemical Society Sectional Meeting, Chemistry of Microcircuit Fabrication, Lexington, Massachusetts, 4 April 1985
6718A	Recent Advances in SOI Films Produced by Zone-Melting Recrystallization	M.W. Geis C.K. Chen H.I. Smith* R.W. Mountain C.L. Doherty	2nd International Workshop on Future Electron Devices, Shuzenji, Japan, 19 March 1985
6758	Integrated-Optical Fiber-Gyroscope Chip Components	L.M. Johnson	OFS '85, San Diego, California, 13 February 1985
6776	Technique for Measuring Surface Diffusion by Laser-Beam-Localized Surface Photochemistry	H.J. Zeiger J.Y. Tsao D.J. Ehrlich	Microphysics of Surfaces, Beams, and Adsorbates, Santa Fe, New Mexico, 4-6 February 1985
6788	A High-Speed Analog Two-Dimensional Gaussian Image Convolver	J.R. Sage A.L. Lattes	OSA Topical Meeting on Machine Vision, Incline, Village, Nevada, 20-22 March 1985
6789	Improved GaAs CCD Spatial Light Modulator Fabrication	B.E. Burke K.B. Nichols R.H. Kingston	OSA Topical Meeting on Optical Computing, Incline Village, Nevada, 18-20 March 1985

* Author not at Lincoln Laboratory.

MS No.			
6792A	Accuracy of Heterodyne and Direct Detection of CO_2 DIAL Systems Detector and Laser Limitations	D.K. Killinger N. Menyuk	ARO Workshop on Remote Sensing for Chemical Defense, Myrtle Beach, South Carolina, 16-18 April 1985
6794	High-Speed Analog Signal Processing with Superconductive Circuits	R.W. Ralston	OSA Topical Meeting on Picosecond Electronics and Optoelectronics, Incline Village, Nevada, 13-15 March 1985
6796	Hybrid Signal Processor for Wideband Radar	I. Yao E.M. Hauser C.A. Bouman A.M. Chiang	
6819	High-Speed Internal Photoemission Detectors Enhanced by Grating Coupling to Surface Plasma Waves	S.R.J. Brueck V. Diadiuk T. Jones W. Lenth	
6802	The Permeable Base Transistor	R.A. Murphy	
6821	High Speed Phenomena in Resonant Tunneling	T.C.L.G. Sollner H.Q. Le C.A. Correa P.E. Tannenwald W.D. Goodhue	
6800	Electronic Structure of Deep-Lying Sulfur Centers in Si	H.J. Zeiger W.H. Kleiner	1985 Spring Meeting of the Materials Research Society, San Francisco, California, 15-18 April 1985
6852	Energy-Beam Techniques for Thin Layers	J.C.C. Fan	
6830	Surface Acoustic Wave Device Modelling Using MSPICE	J.B. Green	Annual Mentor User Group Meeting, Boston, Massachusetts, 26-28 March 1985
6857	Spectral Properties of Semiconductor Diode Lasers	A. Mooradian	Joint Electrical Engineering and Physics Seminar, University of California, Berkeley, California, 8 February 1985

MS No.			
6857A	Spectral Properties of Semiconductor Diode Lasers	A. Mooradian	Norwegian Physical Society, Oslo, Norway, 11-14 April 1985
6872	HgCdTe Infrared Heterodyne Detectors	D.L. Spears	Seminar, Raytheon Research Laboratories, Lexington, Massachusetts, 27 March 1985
6873	Masked Ion Beam Lithography	J.N. Randall	Seminar, Bell Communication, Holmdel, New Jersey, 26 February 1985
6873A	Masked Ion Beam Lithography	J.N. Randall	North Texas Electrochemical Seminar, Garland, Texas, 11 April 1985
6873B	Masked Ion Beam Lithography	J.N. Randall	Seminar, Texas Instruments, Dallas, Texas, 12 April 1985
6889	Millimeter-Wave Monolithic Circuits for Receiver and Transmitter Application	A. Chu W.E. Courtney L.J. Mahoney B.J. Clifton	Electro '85, New York, New York, 23-25 April 1985
6889A	Millimeter-Wave Monolithic Circuits for Receiver and Transmitter Application	A. Chu W.E. Courtney L.J. Mahoney B.J. Clifton	1985 IEEE Princeton Second Sarnoff Symposium, Princeton, New Jersey, 22 March 1985
6898	Wide-band Analog Signal Processing with Superconductive Circuits	R.S. Withers	NASA/DoD Meeting on Millimeter and Submillimeter Waves and Applications, Goddard Space Flight Center, Greenbelt, Maryland, 12 March 1985
6900	Superconductive Dispersive Delay Lines and Application to Spectral Analysis	R.S. Withers A.C. Anderson J.B. Green S.A. Reible	
6915	Beam-Direct-Writing Techniques for Silicon Circuits	B.J. Clifton D.J. Ehrlich	Seminar, Digital Equipment Corporation, Waltham, Massachusetts, 9 April 1985

ORGANIZATION

SOLID STATE DIVISION

A.L. McWhorter, *Head*
I. Melngailis, *Associate Head*
E. Stern, *Associate Head*
J.F. Goodwin, *Assistant*

P.E. Tannenwald, *Senior Staff*

QUANTUM ELECTRONICS

A. Mooradian, *Leader*
P.L. Kelley, *Associate Leader*

Barch, W.E.
Belanger, L.J.
Brueck, S.R.J.
Bushee, J.F., Jr.
DeFeo, W.E.
Feldman, B.
Hancock, R.C.
Harrison, J.*
Johnson, B.C.*
Killinger, D.K.
Menyuk, N.
Sharpe, K.A.

ELECTRONIC MATERIALS

A.J. Strauss, *Leader*
J.C.C. Fan, *Associate Leader*
H.J. Zeiger, *Senior Staff*

Anderson, C.H., Jr.
Button, M.J.
Chen, C.K.
Choi, H.K.
Connors, M.K.
Delaney, E.J.
Fahey, R.E.
Finn, M.C.
Gale, R.P.
Iseler, G.W.
King, B.D.
Kolesar, D.F.
Krohn, L., Jr.
Mastromattei, E.L.
McClelland, R.W.
Nitishin, P.M.
Pantano, J.V.
Tracy, D.M.
Tsaur, B-Y.
Turner, G.W.
Wang, C.A.
Windhorn, T.H.

APPLIED PHYSICS

R.C. Williamson, *Leader*
D.L. Spears, *Assistant Leader*
T.C. Harman, *Senior Staff*
R.H. Rediker, *Senior Staff*

Anderson, K.K.*
Becker, R.A.
Cox, C.H., III
DeMeo, N.L., Jr.
Diadiuk, V.
Donnelly, J.P.
Duffy, P.E.
Ferrante, G.A.
Groves, S.H.
Hovey, D.L.
Johnson, L.M.
Liau, Z.L.
Lind, T.A.
Metze, G.M.
McBride, W.F.
Molter, L.A.*
O'Donnell, F.J.
Plonko, M.C.
Reeder, R.E.
Schloss, R.P.*
Tsang, D.Z.
Walpole, J.N.
Whitaker, N.*
Woodhouse, J.D.
Yap, D.*

---

* Research Assistant
† Part Time

ANALOG DEVICE TECHNOLOGY

R.W. Ralston, *Leader*
R.S. Withers, *Assistant Leader*

Anderson, A.C.
Arsenault, D.R.
Boisvert, R.R.
Bouman, C.A.
Brogan, W.T.
Delaney, M.*
Dolat, V.S.
Fischer, J.H.
Fitch, G.L.
Flynn, G.T.
Green, J.B.
Hauser, E.M.
Holtham, J.H.
Kernan, W.C.
Lattes, A.L.
Macedo, E.M., Jr.
Macropoulos, W.
Marden, J.A.
Melngailis, J.†
Oates, D.E.
Sage, J.P.
Thompson, K.E.†
Yao, I.

MICROELECTRONICS

W.T. Lindley, *Leader*
D.J. Ehrlich, *Assistant Leader*
B.B. Kosicki, *Assistant Leader*
R.A. Murphy, *Assistant Leader*

Astolfi, D.K.
Black, J.G.
Bozler, C.O.
Burke, B.E.
Burke, J.W.
Calawa, A.R.
Chen, C.L.
Chiang, A.M.
Clifton, B.J.
Correa, C.A.
Daniels, P.J.
Durant, G.L.
Efremow, N.N., Jr.
Felton, B.J., Jr.
Geis, M.W.
Goodhue, W.D.
Gray, R.V.
Hollis, M.A.
Lax, B.†
LeCoz, Y.L.*
Lincoln, G.A., Jr.
Lyszczarz, T.M.
Mahoney, L.J.
Manfra, M.J.
McGonagle, W.H.
Mountain, R.W.
Nichols, K.B.
Pang, S.W.
Parker, C.D.
Piacentini, W.J.
Pichler, H.H.
Rabe, S.
Randall, J.N.
Rathman, D.D.
Reinold, J.H.
Rothschild, M.
Sedlacek, J.H.C.
Smythe, D.L., Jr.
Sollner, T.C.L.G.
Sullivan, D.J.
Taylor, J.A.*
Vera, A.
Wilde, R.E.

---

* Research Assistant
† Part Time

1. SOLID STATE DEVICE RESEARCH

1.1 INTEGRATED-OPTICAL FIBER GYROSCOPE COMPONENTS

Integrated-optical circuits are being developed for fiber gyroscope systems. These circuits could be utilized to reduce both system size and complexity, as well as to improve system performance. One circuit design is shown in Figure 1-1 and includes a double-Y waveguide branching structure, polarizer, phase modulator and frequency shifter. The frequency shifter allows wide system dynamic range by introducing a frequency difference between the counter-propagating beams to null out the rotation-induced phase shift. The phase modulator is used to maintain high sensitivity by introducing an additional $\pi/2$ nonreciprocal phase shift. Here, we report on the progress in investigating the design and performance in $LiNbO_3$ of two of these circuit components: the double-Y branch and a serrodyne optical frequency translator.

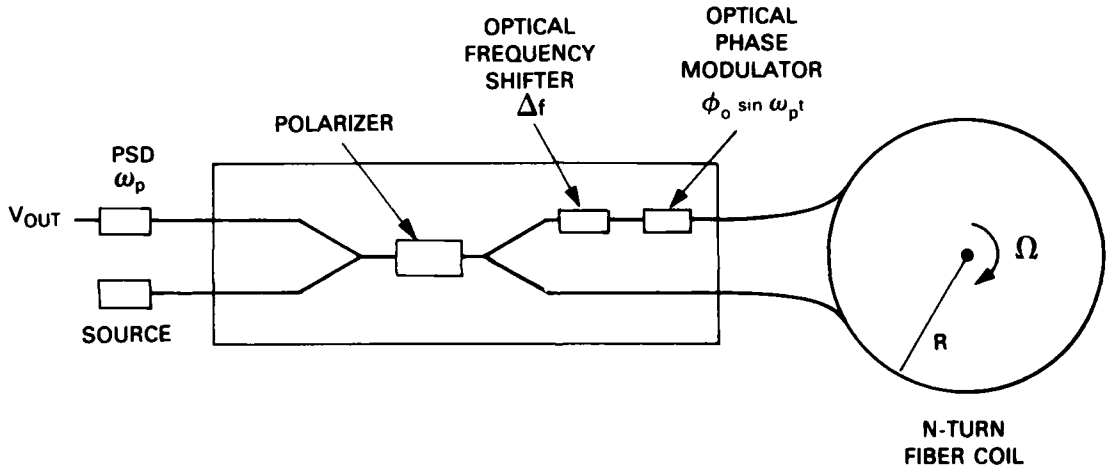

143336-N-02

Figure 1-1. Integrated optical chip design for fiber gyroscope system.

Insertion loss is an important performance parameter for fiber gyroscope components. Branching structures, which are required for many components, have two primary loss mechanisms: a combined splitting and curvature loss and a scattering loss. Here, we have fabricated a double-Y branch using the design shown in Figure 1-2. A small branching angle and closely spaced coherently coupled 0.2° bends[1] are used to maintain low insertion loss and to obtain a guide separation of 140 μm over a chip length of only 5.3 mm. The two Y-branches are separated by a 1-cm-long guide, and the entire chip is 6.3 cm long. We have previously shown that the bending loss through a series of closely spaced coherently coupled bends is significantly lower than the loss through a comparable number of isolated bends. Here, the bend spacing is 200 μm.

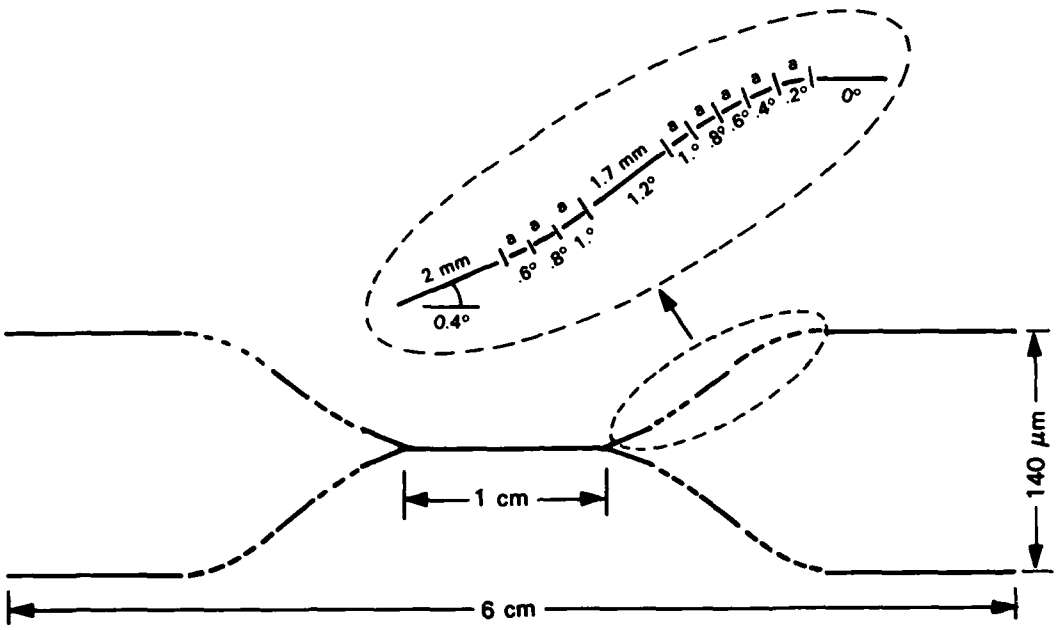

Figure 1-2. Double-Y waveguide branching circuit utilizing coherently coupled waveguide bends.

The guides were fabricated to provide single-mode operation at 0.85 μm on X-cut $LiNbO_3$ with propagation in the Y direction. The devices were tested by end-fire coupling TE-polarized light from a 0.85-μm diode laser. By comparing the transmission of double-Y branches with straight guides fabricated on the same substrate, the excess loss due to the bends and branches was determined to be only 0.5 dB. The two outputs of the circuit were equal to within 1 dB. The total insertion loss, measured by coupling a single-mode polarization-preserving fiber to one end of the double-Y circuit and a conventional single-mode fiber to the opposite end, was determined to be only 6 dB in excess of the 6-dB loss of an ideal device. We estimate the propagation loss of this structure to be 4.5 dB and the fiber-coupling loss to be 1.0 dB. The propagation loss should be much lower in a similar circuit designed for 1.3-μm operation. We have recently measured a total-insertion loss at 1.3 μm of less than 1 dB through a straight 2.3-cm-long fiber-coupled single-mode waveguide.

Serrodyne optical frequency translation, using $LiNbO_3$ channel-waveguide phase modulators, has also been investigated. Ideal single-sideband serrodyne frequency translation can be obtained by phase-modulating an optical signal with a sawtooth with zero fall time and an amplitude equal to an integral number of 2π radians. A $LiNbO_3$ Mach-Zehnder waveguide interferometer, as shown in Figure 1-3, was used to investigate the serrodyne technique. By applying sawtooth signals at frequencies Δf_1 to one arm and Δf_2 to the other arm, where $\Delta f_1 >> \Delta f_2$, it is possible to observe both the upper and lower sidebands of the frequency shifted signal Δf_2 about Δf_1. For this experiment, Δf_2 = 60 kHz and Δf_1 = 2 kHz. Both signals had a 1% fall time. Figure 1-4 exhibits the output power spectrum for the case where the 2-kHz sawtooth voltage has been

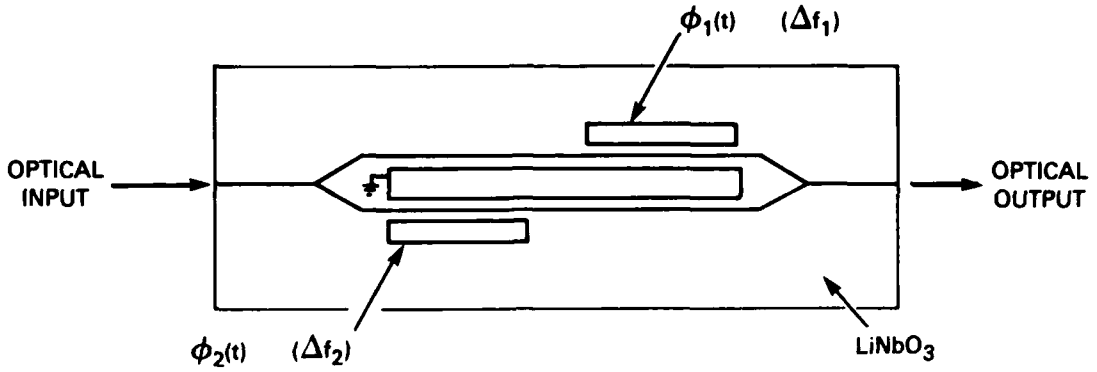

148426-N-02

Figure 1-3. Mach-Zehnder waveguide interferometer for evaluating serrodyne frequency translation.

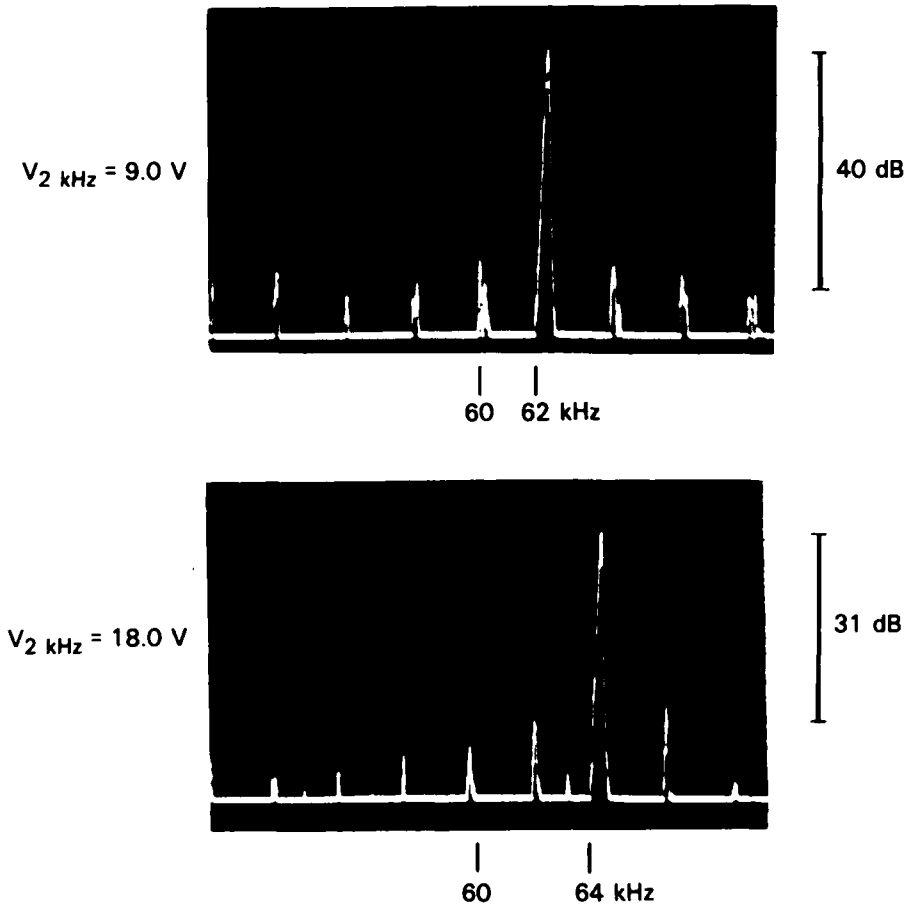

148863-R-01

Figure 1-4. Output power spectrum from interferometer with 60 kHz and 2 kHz sawtooth signals applied to opposite electrodes.

adjusted for maximum sideband suppression. There is ≈ 100% conversion efficiency and the sideband suppression is ≈ 40 dB. Since these devices are polarization sensitive, this result indicates there is little mode conversion occurring within the modulator. Similar results have also been obtained for frequency shifts up to 100 kHz.

L.M. Johnson

1.2 HIGH-FREQUENCY RESPONSE OF SMALL-CONTACT MASS-TRANSPORTED INJECTION LASERS

The small-signal high-frequency performance of diode lasers is of interest for the distribution of microwave signals over optical fibers. The response of 1.3-μm lasers is often limited by a parasitic contact pad capacitance.[2] This capacitance is formed in most laser structures by the contact pad metallization and a thin electrical insulator which overlaps the substrate material in areas outside of the actual laser stripe. The frequency response of the lasers was shown to improve as this parasitic capacitance was reduced.[2] We report initial results taken on small-contact mass-transported lasers in which the area of the contact is limited to the laser mesa and the parasitic pad capacitance is eliminated.

The lasers were fabricated using the mass-transport process as described previously.[3] Figure 1-5 illustrates a cross-sectional view of the mass-transported laser. The GaInAsP active region was 2 μm wide and 0.15 μm thick. On each side of the active region were 3.5-μm-wide regions of mass-transported InP, which formed the buried heterostructure. Contact metallization was photolithographically confined to a 4-μm-wide stripe above the 6-μm laser mesa, as shown in Figure 1-5. The lasers were In-soldered in a microstripline package with the stripe side up. In-coated Au ribbons were used to connect the microstripline to the contact stripe.

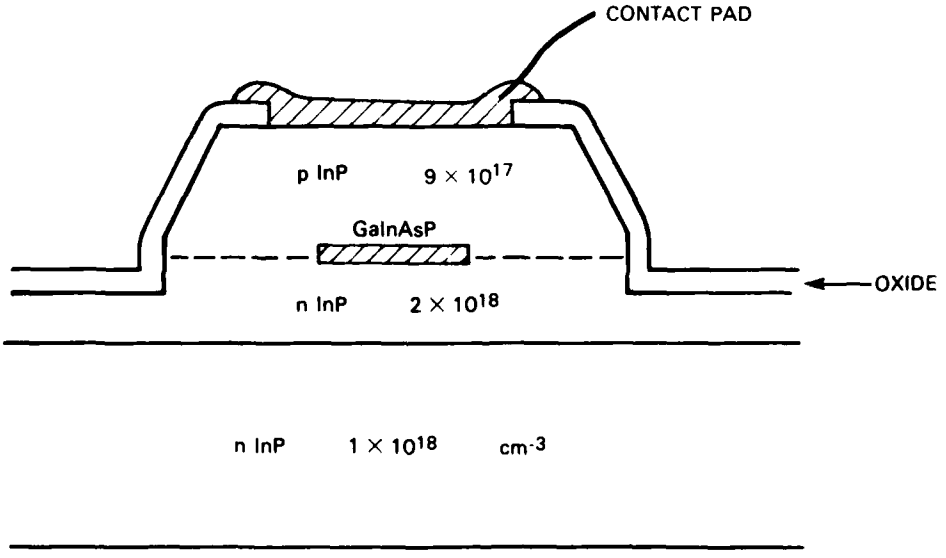

Figure 1-5. Schematic cross section of small contact mass-transported diode laser. Contact is confined to top of mesa to eliminate parasitic contact pad capacitance.

The microwave impedance of the diode is primarily capacitive at zero bias. With forward bias, the capacitance is shorted as the diode begins to conduct and the impedance of the laser is 10 Ω up to a frequency of 7 GHz, above which lead inductance (about 0.25 nH) begins to dominate the impedance. The electrical impedance does not change with current once the diode conducts.

Frequency response measurements were made using a network analyzer with a reflection-transmission test set. The laser was connected to the output of the test set and an InGaAs detector, with a 3-dB roll-off frequency of 8 GHz, was connected to the input. The laser emission was collected with a 0.6-NA lens and focused onto the detector with a 0.5-NA lens. A wideband bias network was placed between the reflection-transmission test set and the laser without impedance matching. RF insertion loss between the input to the laser and the detector output was measured over the 0.1 to 8 GHz range using the leveled output of a sweep oscillator to drive the laser.

Figure 1-6(a) through (c) shows frequency response of a 400 μ-long device for different values of DC bias current. Pronounced response peaks associated with the laser relaxation oscillation frequency are evident, they are not observed for lasers with large parasitic capacitance. The amplitude of this peak increases with increasing current, peaks at about 40 mA, and decreases with higher currents. The ratio of the power at the resonant frequency to the power at low frequencies is shown as a function of the square root of the DC optical power in Figure 1-7. With low parasitic capacitance, the response is enhanced by as much as 10 dB at this resonant frequency.

The resonant frequency increases with DC bias current and the resonant peak broadens considerably. At 30 mA, just above the 25-mA threshold current, the resonance occurs at 1.4 GHz. At 90 mA the peak occurs at about 5 GHz and the response is 3 dB down from the low-frequency value at about 6 GHz. This 3-dB roll-off frequency is plotted as a function of the square root of the DC optical power in Figure 1-7 and shows an approximate linear dependence.

At low frequencies (100 MHz) the total microwave insertion loss, from the input of the laser bias network to the detector output, was about 23 dB and this low-frequency insertion loss was independent of DC bias from just above the 25-mA threshold current to about 50 mA. At higher DC biases the efficiency of the laser decreases as a result of current leakage around the active layer and heating.

Initial results on these lasers indicate that longer lasers have better high-frequency performance because of higher optical power output. Measurements of a 150-μm laser show a maximum relaxation oscillation frequency of only 3.3 GHz. The output power of this 150-μm laser began to saturate near 2.5 mW, whereas the 400 μm laser did not saturate up to 8 mW. At equivalent output power, the shorter laser did have a higher relaxation oscillation frequency, as expected.

Comparisons of our results with other 1.3-μm lasers show that our relaxation frequencies are similar to those seen in other buried heterostructure lasers[2] and higher than those reported for ridge waveguide[2] and DC-PBH[4] structures. However, a 12.5-GHz relaxation oscillation frequency has been reported[5] for short-cavity vapor-phase-regrown lasers operated on a pulsed basis. Compared to the small-contact mass-transported lasers reported here, the vapor-phase regrown lasers

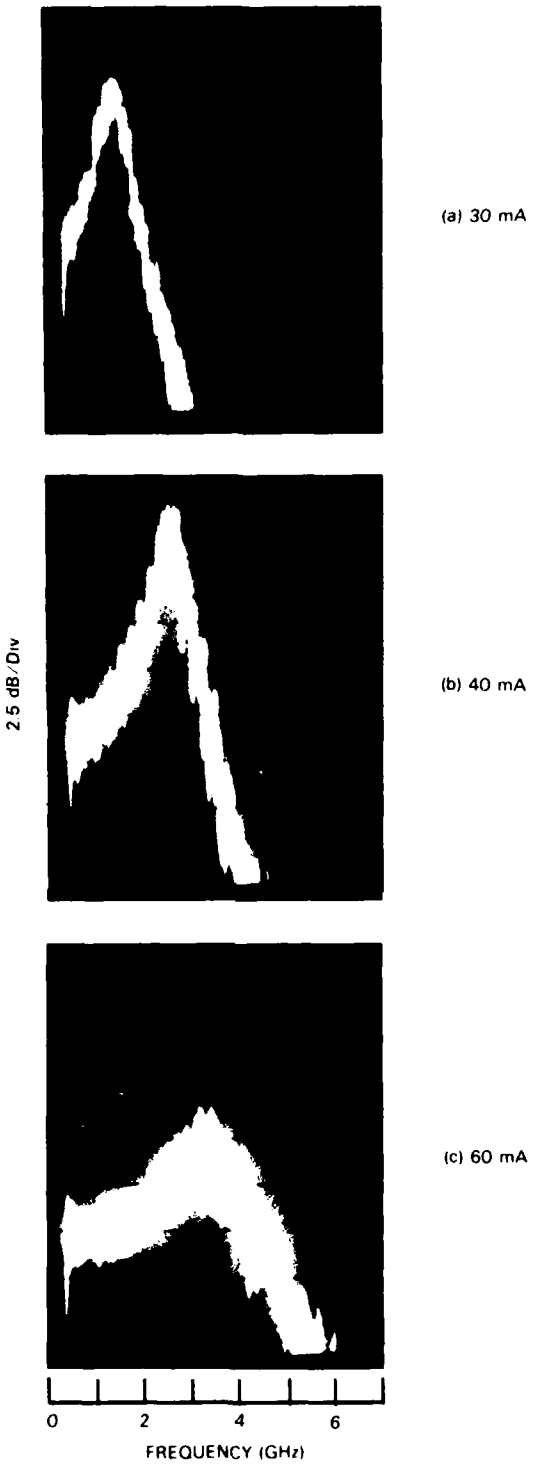

Figure 1-6. Small-signal frequency response of a 400-μm-long laser for different DC injection current levels. The laser threshold of this device is 25 mA.

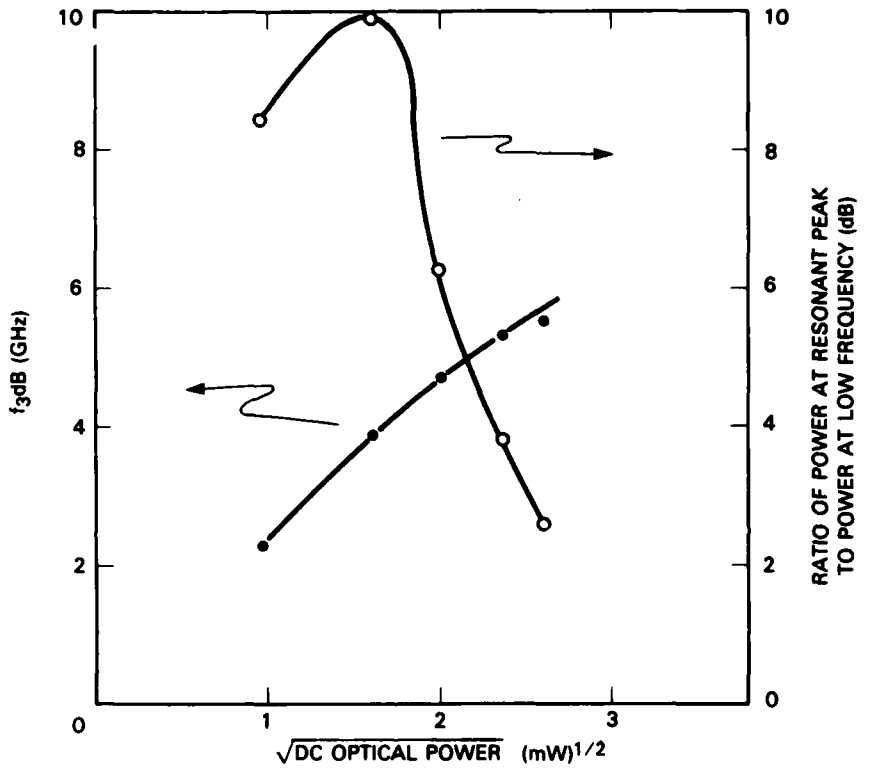

152302-N-01

Figure 1-7. Dependence of resonant peak amplitude and frequency response on DC optical power for the 400-μm laser used in Figure 1-6.

were twice as wide and twice as thick, and had twice the doping level in the InP cap and over three times the output power per unit length. However, transverse and lateral mode quality tend to be compromised in lasers with thick and wide active regions. We are investigating means to increase the high-frequency performance of buried heterostructure lasers while preserving lowest order mode quality.

D.Z. Tsang
Z.L. Liau

REFERENCES

1. L.M. Johnson and F.J. Leonberger, Opt. Lett. **8**, 111 (1983).
2. R.S. Tucker and I.P. Kaminow, J. Lightwave Technol. **LT-2**, 385 (1984).
3. Z.L. Liau, J.N. Walpole, and D.Z. Tsang, IEEE J. Quantum Electron. **QE-20**, 855 (1984).
4. I. Mito, M. Kitamura, M. Yamaguchi, K. Kobayashi, and I. Takano, Electron. Lett. **20**, 261 (1984).
5. C.B. Su, V. Lanzisera, W. Powazinik, E. Meland, R. Olshansky, and R.B. Lauer, Appl. Phys. Lett. **46**, 344 (1985).

2. QUANTUM ELECTRONICS

2.1 HIGH-SPEED INTERNAL PHOTOEMISSION DETECTORS ENHANCED BY GRATING COUPLING TO SURFACE PLASMA WAVES

In previous contributions,[1,2] we reported on the use of grating coupling to surface plasma waves (SPW) to enhance the quantum efficiency of internal-photoemission detectors in which hot carriers, generated in a metal film by optical absorption, are collected by photoemission over a Schottky barrier into a semiconductor. This class of detectors is of interest as a result of its uniformity, high-speed potential, long wavelength response with binary rather than quaternary III-V compounds, and compatibility with integrated circuit fabrication techniques.[3-5] The response speed of these detectors is generally limited by the RC time constant associated with the Schottky barrier depletion region and by the carrier transit time across this depletion region; relaxation processes within the metal and the semiconductor are in the subpicosecond range and do not limit detector response. High-saturation-velocity III-V semiconductors can be used to minimize transit time effects. Here, we report measurements of the limiting response speeds of Au-(p-InP) internal-photoemission detectors fabricated on substrates textured with shallow gratings to enhance the coupling into the SPW modes of the metal film.

Photolithography and wet chemical etching were used to fabricate gratings with 2-μm period and 1:3 line:space ratio on p-InP substrates with doping concentrations ranging from 10^{16} - 10^{18} cm^{-3}. Thin (30-50 nm), electron-beam evaporated, Au films were deposited to form the Schottky barriers. Fabricated detectors ranged from 67 to 150 μm in diameter. Thermally evaporated AuMg, alloyed at 420°C for 10 s, provided the ohmic back contact.

The coupling to surface plasma waves can be monitored by measuring the detector response to monochomatic radiation as a function of the angle of incidence. At the appropriate angle for coupling into a SPW, there is a substantial increase in the responsivity.[1,2] These angular responsivity curves are very sensitive to the precise details of the grating and film parameters. An example of this sensitivity is given in Figure 2-1 which shows the angular response pattern at 1.15 μm for two detectors with a 50-nm-deep grating. The only difference in the fabrication was that one detector (a) had a 30-nm-thick Au film while the second detector (b) had a 50-nm-thick Au film.

The three peaks in the responsivity for detector (a) correspond to second, first, and third order coupling to the SPW bound to the air-Au interface as θ is increased. Reflectivity measurements indicate that approximately 10-15% of the incident power is coupled out of the zero-order (dominant) reflected beam at these angles. Model calculations, based on a Raleigh approximation perturbative treatment, indicate that only about 1/3 of this power is coupled into the SPW, while the majority is redistributed among the various diffracted orders and radiated away. This coupling will be improved by using a higher spatial frequency grating so that only one order of the grating couples the incident light into the SPW and there are no additional diffracted beams. Under appropriate conditions,[6] nearly 100% of the incident energy can be coupled into the SPW.[6]

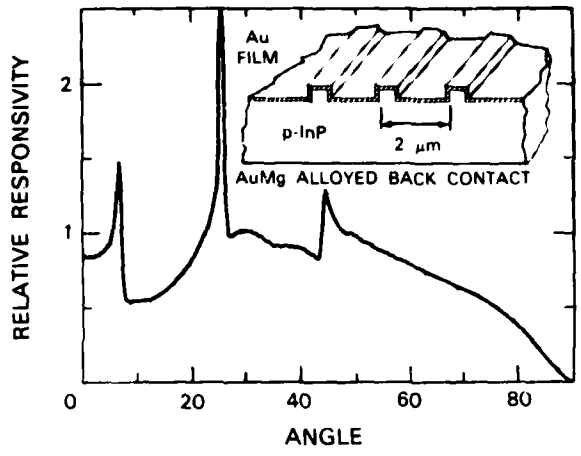

(a)

143442-N-04

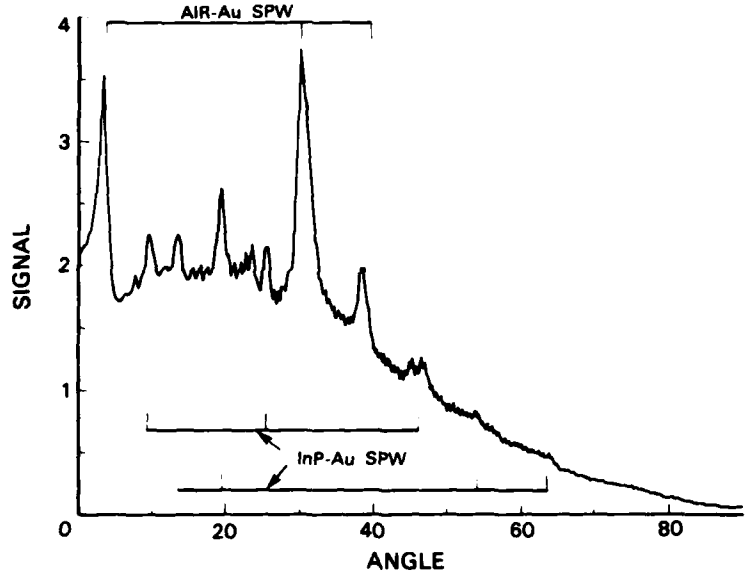

(b)

148227-N-01

Figure 2-1. Angular dependence of the responsivity for two 50-nm-deep grating detectors. Detector (a) has a 30-nm-thick Au film while detector (b) has a 50-nm-thick film. Note the extra peaks, corresponding to coupling to the Au-InP surface plasma wave, evident for detector (b).

The detector with the thicker Au film (b) exhibits a much more complex angular response pattern; there are now at least 10 peaks which arise from coupling to the surface modes at both the air-Au interface, as in the previous example, and the Au-InP interface. This second mode has a much larger wave vector, corresponding to the high refractive index of the InP; the coupling is

controlled by higher spatial harmonics (5 through 8) of the fundamental grating profile. Consequently, these couplings were very sensitive to the sharpness of the grating edges and the presence of small-scale roughness and were not readily reproducible for nominally identical detectors. The two sets of coupling angles indicated for the Au-InP interface arise because of reflection of the optical beams transmitted through the Au film from the back surface of the InP material. These responsivity curves are more sensitive to energy absorbed at the Au-InP interface since the hot carriers do not have to diffuse across the metal film before collection. As a result of the longer penetration depth of the optical field into the metal for the Au-InP mode than for the air-Au mode, the effects of coupling to this Au-InP surface mode were not as evident for the thinner film. Modifying the groove depth also results in dramatic changes in the angular responsivity patterns. The narrow responsivity peaks become plateaus for 100-nm-deep grooves, as discussed elsewhere.[2] The angular span of these plateaus can be adjusted to match the output radiation pattern of optical fibers.

The speeds of these devices were limited by RC effects involving capacitance of the depletion region and the resistance of the back contact. This is illustrated in Figure 2-2, which shows the RC time constant (solid line) evaluated from the measured forward bias resistance (400 Ω) and the measured Schottky barrier capacitance vs reverse bias voltage for a detector with a 125-μm diameter active area and a hole concentration of 1×10^{16} cm^{-3}. The dashed curve is an extrapolation of the RC limit to higher bias voltages. Also shown are the measured device response times to ~150-ps-duration 1.06-μm pulses from a CW-mode-locked YAG laser. The two sets of measurements are in agreement.

It is also interesting to compare the response time of the same detector for irradiation at 1.06 μm, where the detection mechanism is SPW-enhanced internal photoemission, and for above-band gap irradiation at 570 nm, where electron-hole pair generation within the depletion region dominates the responsivity. This comparison is shown in Figure 2-3 for a 20-V reverse bias, where the response to 150-ps-duration 1.06-μm pulses is shown on the left side and the response to 3-ps 570-nm pulses is on the right. The rise times of the signals vary as a result of the differing laser pulse widths; the fall times are identical and reflect the detector RC time constant.

Improvements in both the detector response speed and the quantum efficiency will enhance the utility of these internal photoemission detectors.The RC-limited decay times can be reduced by decreasing the capacitance using smaller areas and lower carrier concentrations (longer depletion widths). There is a lower limit to the detector area set by the SPW mean free path. For smaller detectors, the enhancement due to the SPW coupling is reduced. These effects were observed using 67-μm-diameter detectors, which had decay times of less than 100 ps, but whose angular response patterns showed reduced coupling and overall lower responsivities. Improvements in the detector time response can also be achieved by decreasing the back contact resistance; experiments using Zn skin diffusions to improve this resistance are in progress.

The detector quantum efficiency should be improved by illuminating the detector through the substrate and coupling to the SPW mode at the Au-InP boundary. Hot carriers would not be

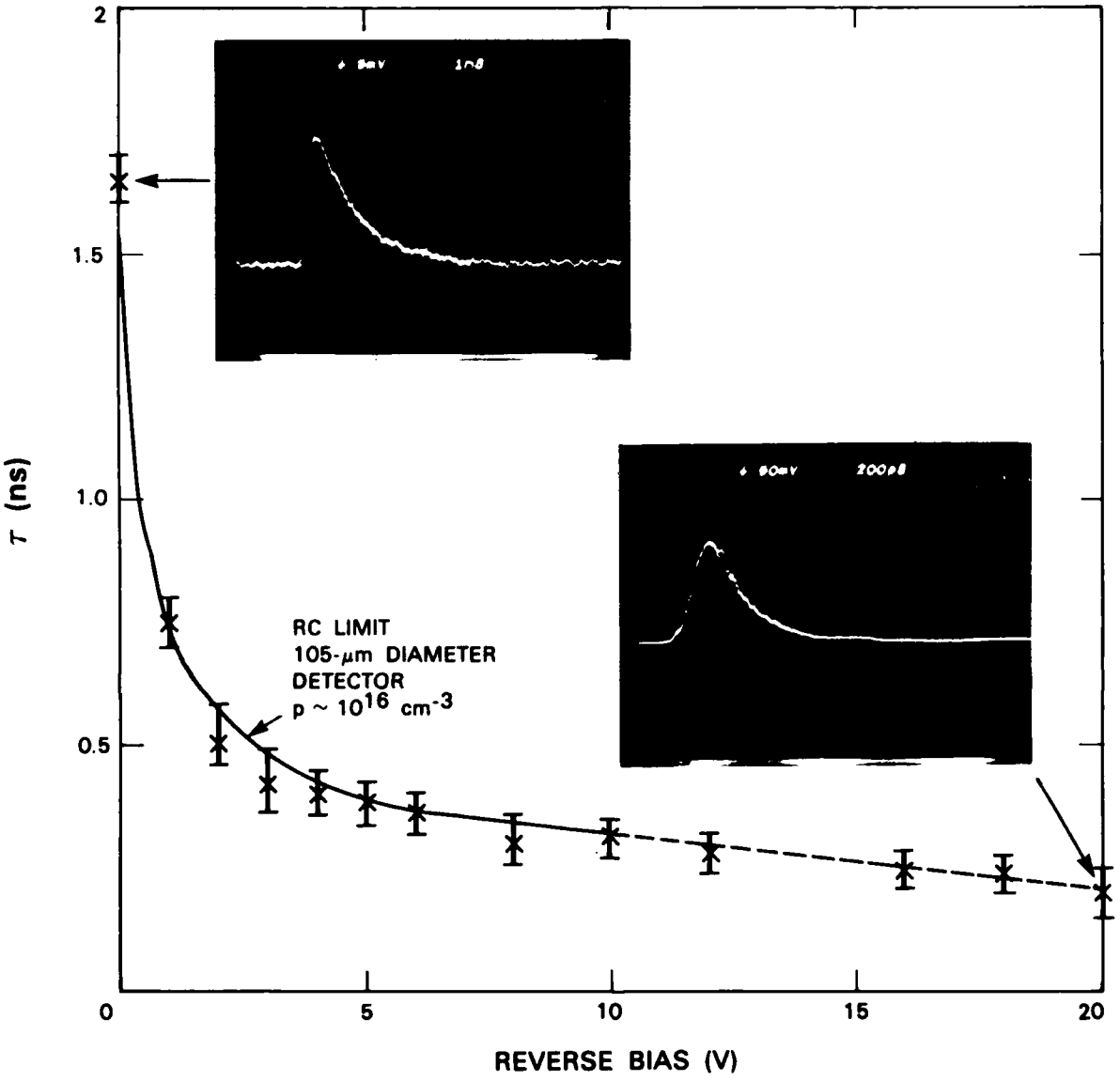

Figure 2-2. Measured RC time constant limit (solid curve) and temporal response times (points) for a 125-μm-diameter detector.

1.06 μm
150-ps DURATION PULSE

570 nm
3-ps DURATION PULSE

149228-R

Au-InP DETECTOR
125-μm DIAMETER
$p \sim 1 \times 10^{16}$ cm^{-3}
BIAS -20 V

Figure 2-3. Detector response at a 20-V reverse bias for below band gap 1.06-μm radiation (left, 150-ps pulse duration) and for above band gap radiation at 570 nm (right, 3-ps pulse duration).

required to diffuse across the metal film before collection. In addition, thicker Au films with better coupling to the SPW would be possible. For the present detectors, where the metal film thickness is limited to a hot-carrier diffusion length, optimal coupling is not achieved and less than 10% of the incident radiation is coupled into the surface mode. Higher spatial frequency gratings (period $\sim\lambda/n$, where n is the InP refractive index) are required to insure optimum coupling to this SPW.

S.R.J. Brueck
V. Diadiuk

REFERENCES

1. S.R.J. Brueck, V. Diadiuk, T. Jones and W. Lenth, Appl. Phys. Lett. (to be published).
2. Solid State Research Report, M.I.T. Lincoln Laboratory, (1984:4), DTIC AD158013.
3. F.D. Sheperd, in *Infrared Detectors*, W.L. Wolfe, Ed., Proc. SPIE **43**, 42 (1984).
4. W.F. Kosonocky and H. Elabd, in *Infrared Detectors*, Proc. SPIE **43**, 167 (1984).
5. R.C. McKee, IEEE Trans. Electron Devices, **ED-31**, 968 (1984).
6. G.N. Zhizhin, M.A. Moskalova, E.V. Shomina and V.A. Yakovlev, in *Surface Polaritons*, V.M. Agranovich and D.L. Mills, Eds. (North-Holland, New York, 1982).

3. MATERIALS RESEARCH

3.1 ROOM-TEMPERATURE OPERATION OF GaAs/AlGaAs DIODE LASERS FABRICATED ON A MONOLITHIC GaAs/Si SUBSTRATE

As Si integrated circuits increase in complexity, packing density, size, and speed, there is increasing interest in replacing the wire interconnects between Si subsystems with high-data-rate optical interconnects. The use of optical interconnects will require the integration of Si and III-V components and circuits, since optical sources cannot be fabricated from Si. One approach to such integration is the fabrication of diode lasers or light-emitting diodes in layers of III-V compounds grown directly on Si wafers. We recently reported[1] the first operation of diode lasers fabricated on a monolithic GaAs/Si (MGS) substrate. Those lasers, which were double-heterostructure devices with an AlGaAs active layer, were limited to pulsed operation at 77 K with maximum power output of 1.8 mW/facet. We now report the first room-temperature operation of diode lasers fabricated on an MGS substrate. For these new devices, which incorporate an asymmetric large optical cavity (LOC), threshold currents as low as 775 mA, power outputs up to 27 mW/facet, and differential quantum efficiencies up to 2.8% per facet have been obtained in pulsed operation at room temperature.

The cross-sectional structure of the new MGS diode lasers, which are oxide-defined stripe geometry devices, is shown schematically in Figure 3-1. The following GaAs and AlGaAs layers were grown by molecular beam epitaxy on a (100) p-Si (~1 Ω cm) wafer: a 9-μm n^+-GaAs buffer layer, a 2.1-μm n^+-$Al_{0.5}Ga_{0.5}As$ outer confinement layer, a compositionally graded 0.25-μm

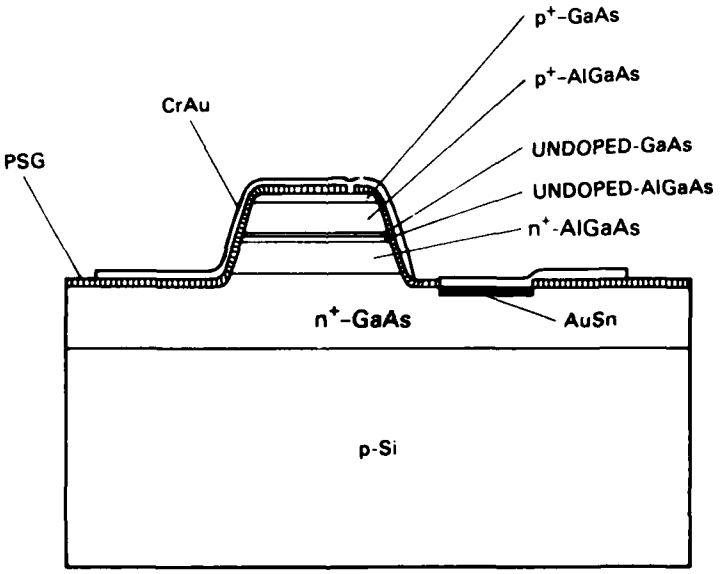

151566-N

Figure 3-1. Schematic illustration showing cross-sectional structure of GaAs/AlGaAs MGS diode lasers.

undoped AlGaAs separate confinement layer and a 0.15-μm undoped GaAs active layer forming the LOC, a 1.7-μm p^+-$Al_{0.5}Ga_{0.5}As$ confinement layer, and a 1.5-μm p^+-GaAs cap layer for electrical contact. Si and Be were used as the n- and p-type dopants, respectively.

The device fabrication procedure was somewhat different from that used for the previous MGS diode lasers. Chlorine-assisted ion beam etching[2] was used to form 100-μm-wide, 3.5-μm-deep channels on 400-μm centers. Scanning electron microscopy revealed that the channels had vertical walls with numerous small vertical striations, which are typically obtained by ion beam etching. A short etch in a room-temperature mixture of hydrochloric acid, hydrogen peroxide, and water was used to improve the smoothness of the channel walls and to remove the remaining AlGaAs. Grooves 400-μm wide on 500-μm centers, which exposed the buffer layer, were then formed perpendicular to the ion-beam-etched channels by wet chemical etching. This procedure yielded rectangular (100 μm $\times$ 300 μm) mesas surrounded on all four sides by the exposed GaAs buffer layer, with the vertical channel walls serving as end mirrors of optical resonators 300-μm long. The entire wafer was then coated with pyrolytically deposited phosphosilicate glass (PSG). Contact windows were opened in the PSG layer within the etched grooves, and AuSn contact pads were deposited on the exposed buffer layer by electron beam evaporation and photolithographic lift-off. Stripe contact windows (4 μm $\times$ 300 μm) were then opened in the PSG on the mesas. Large-area Cr-Au contact pads were deposited over the stripe windows and the AuSn buffer contacts by evaporation and lift-off. Finally, the wafer was diced into individual device chips.

Twenty randomly chosen devices were evaluated at room temperature by applying 60 ns bias pulses at a repetition rate of ~4 kHz. Stimulated emission was obtained in 17 cases. The power output as a function of current for a typical device is plotted in Figure 3-2. The threshold current (I_{th}) for most devices was between 1.0 and 1.15 A. The lowest I_{th} was 775 mA. Power outputs from 6.5 to 14.4 mW/facet were measured at 1.5 I_{th}. Maximum power outputs ranged from 9 to almost 27 mW/facet at currents of 1.9 to 3.5 times I_{th}. The highest differential quantum efficiency was 2.8% per facet.

Emission spectra for a typical device at three current values are shown in Figure 3-3. The separation between successive emission peaks is ~ 3 Å, consistent with multiple longitudinal mode oscillation in a cavity 300-μm long. At low current values the dominant emission peak for this and most of the other devices was near 8700 Å, closely corresponding to the 1.42 eV bandgap of the GaAs active region. With increasing current the dominant peak exhibited an unexplained shift to higher energies.

The great improvement in performance of the new MGS diode lasers compared with the earlier ones[1] can be attributed to improvements in material quality, device design, and fabrication procedure. These improvements include reducing the stripe width from 8 μm to 4 μm, increasing the AlAs content of the outer confinement layers from 30 to 50 mole percent to obtain better optical confinement, and utilization of an LOC structure to obtain better carrier confinement in

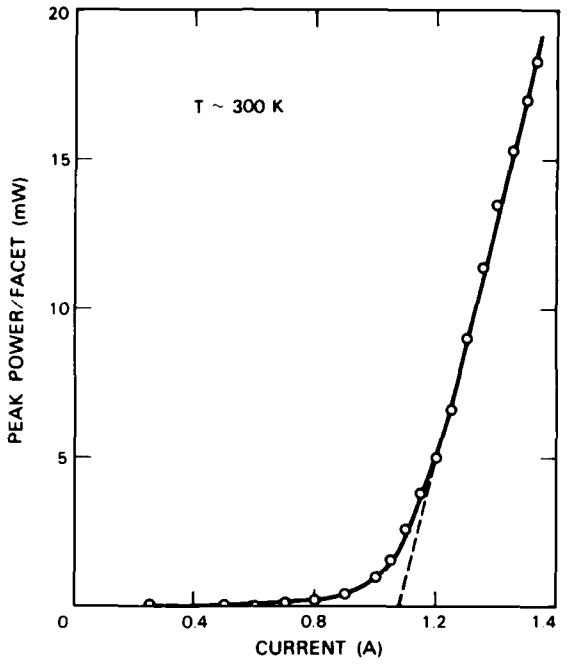

151568-N

Figure 3-2. Power emitted from one facet of a typical MGS diode laser as a function of current for pulsed operation at 300 K.

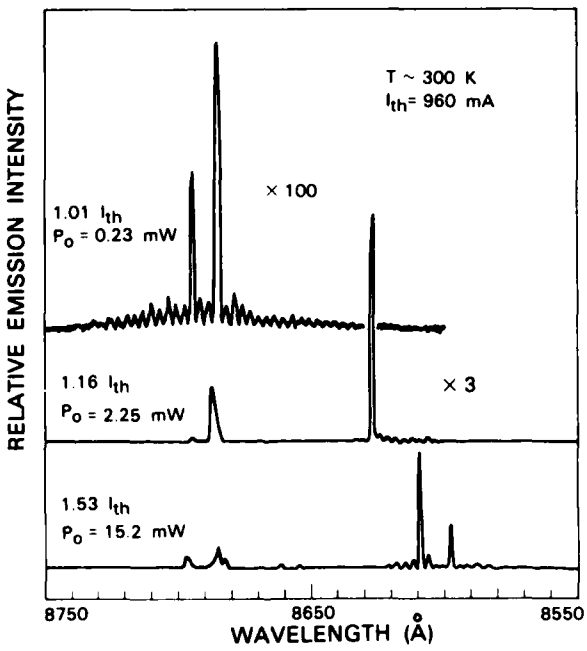

151567-N

Figure 3-3. Emission spectra for a typical MGS diode laser.

the GaAs active layer, all of which tend to reduce I_{th}. The higher AlAs content of the outer confinement layers and the improved mirror quality achieved by chemical etching contribute to the improvement in differential quantum efficiency.

T.H. Windhorn
C.M. Metze

3.2 DETRIMENTAL OPTICAL PROPERTIES OF GERMANIUM INTERMEDIATE LAYERS IN MONOLITHIC TANDEM SOLAR CELL STRUCTURES

There is extensive current interest in the development of tandem solar cells, which have the potential of achieving higher conversion efficiencies than those attainable with single-junction cells. One proposed monolithic tandem structure consists of an upper GaAs or GaAlAs cell, a thin intermediate Ge layer (used to improve the crystal quality of the GaAs or GaAlAs), and a lower Si cell. Any optical losses due to the Ge layer will reduce the photocurrent of the Si cell and therefore decrease the overall conversion efficiency. No estimate of these losses has been reported. To establish lower limits for such losses, we have used the bulk optical constants of single-crystal Ge at 300 K to calculate the transmission of the Ge layer as a function of thickness for the region of the AM1.5 solar spectrum between the absorption edges of the upper and lower cells. The results of the calculations show that the Ge layer must be extremely thin in order to avoid significant reduction in efficiency.

The calculations were performed for the structure shown schematically in Figure 3-4; it consists of an upper GaAs or $Ga_{0.72}Al_{0.28}As$ layer (designated as medium 1), a Ge layer (medium 2)

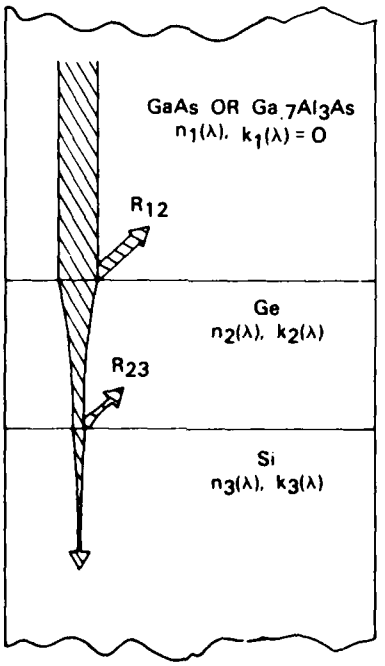

141676-N

Figure 3-4. Schematic tandem solar cell structure.

of thickness d, and a Si substrate (medium 3), with solar radiation normally incident on the upper surface of medium 1. It was assumed that medium 1 absorbs all of the radiation with photon energies exceeding its energy gap (E_{g1}), but that it causes no attenuation for photon energies less than E_{g1}. The transmission (T) of the Ge layer was evaluated for photon energies between E_{g1} and the energy gap of Si (E_{g3}); the results were used to determine how much the optical losses due to the Ge layer reduce the photocurrent of the Si cell in the GaAs/Ge/Si and $Ga_{0.72}Al_{0.28}As$/Ge/Si tandem structures.

Two sets of transmission calculations were performed. One set utilized the following simple expression:

$$T = (1 - R_{12})(1 - R_{23})\, A_2 , \tag{3-1}$$

where R_{12} is the reflection at the interface between the GaAs or GaAlAs layer and the Ge layer, R_{23} is the reflection at the Ge-Si interface, and A_2 is the single-pass absorption of the Ge layer. The absorption term is given by

$$A_2 = \exp(-\alpha_2 d) , \tag{3-2}$$

where α_2 is the absorption coefficient of Ge at wavelength λ.

Equation (3-1) is convenient because it allows a clear separation between the effects of absorption and reflection. This expression is not exact, however, since it does not take into account the interference effects produced by multiple passes of radiation through the Ge layer. Our second set of transmission calculations utilized the complete expression[3] for transmission through an absorbing film bounded by two different media:

$$T = \frac{\gamma_1}{\gamma_3} \frac{[(1 - R_{12})(1 - R_{23}) - 4\sqrt{R_{12}R_{23}} \sin \delta_{12} \sin \delta_{23}]\, e^{-2(\beta_2 - \beta_3)d}}{1 + 2\sqrt{R_{12}R_{23}}\, e^{-2\beta_2 d} \cos(\delta_{12} + \delta_{23} + 2\alpha_2 d) + R_{12}R_{23}e^{-4\beta_2 d}} , \tag{3-3}$$

where

$$\delta_{12} = \arctan \frac{-2(\gamma_1\beta_2)}{\gamma_1^2 - (\gamma_2^2 + \beta_2^2)} ,$$

$$\delta_{23} = \arctan \frac{2(\gamma_3\beta_3 - \gamma_2\beta_3)}{(\gamma_2^2 + \beta_2^2 - (\gamma_3^2 + \beta_3^2)} ,$$

$\gamma_i = 2\pi n_i/\lambda$ and $\beta_i = 2\pi k_i/\lambda$, with n_i the index of refraction and k_i the extinction coefficient for medium i at wavelength λ.

For the AM1.5 photon energies in the 1-2 eV range, Equations (3-1) and (3-3) were used to calculate the transmission through Ge layers of different thicknesses in the structure of Figure 3-4. The values of T obtained for selected values of d between 0.01 and 0.5 μm are plotted in Figure 3-5. Because of the high values of α_2, the relative differences between the approximate and exact T values are small. The maximum difference, averaged over all wavelengths, occurs for d = 0.5 μm and is only 6.4%.

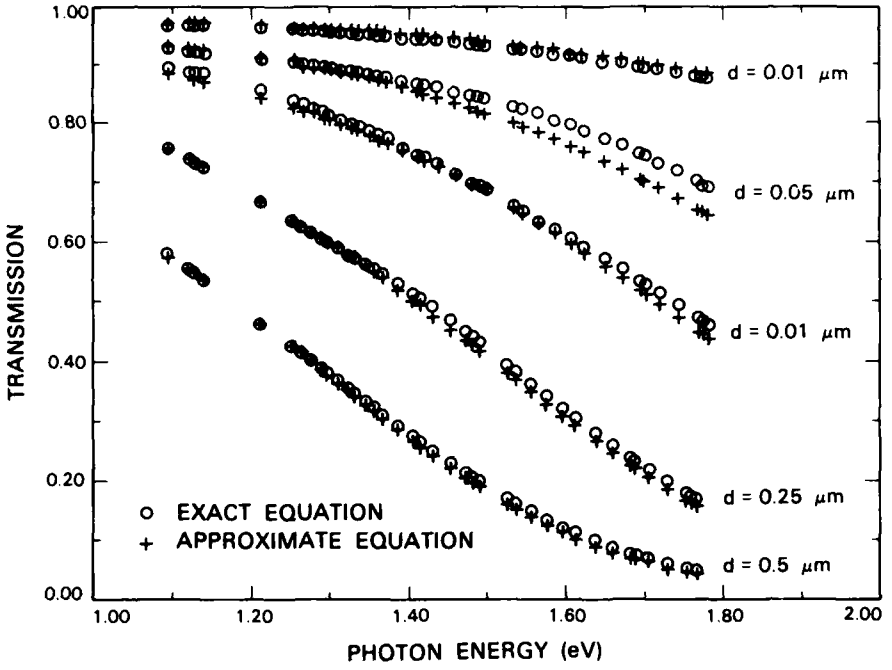

Figure 3-5. Transmission vs photon energy for various Ge layer thicknesses calculated using the exact and approximate expressions.

The T values of Figure 3-5 were used to determine the effect of optical losses due to the Ge layer on the Si cell photocurrent in the GaAs/Ge/Si and $Ga_{0.72}Al_{0.28}As$/Ge/Si structures. For each structure and each value of d, the photocurrent flux per unit wavelength at each of the appropriate wavelengths of the AM1.5 spectrum was calculated by multiplying the photocurrent flux for d = 0 by the calculated T value. The photocurrent density for the Si cell was then found by summing the flux values for the different wavelengths, and the fractional photocurrent for the cell was determined by taking the ratio of this density to the photocurrent density for d = 0. The results are shown in Figure 3-6, where the fractional photocurrents are plotted as a function of d. The fractional photocurrents obtained by using the approximate and exact T values are in excellent agreement.

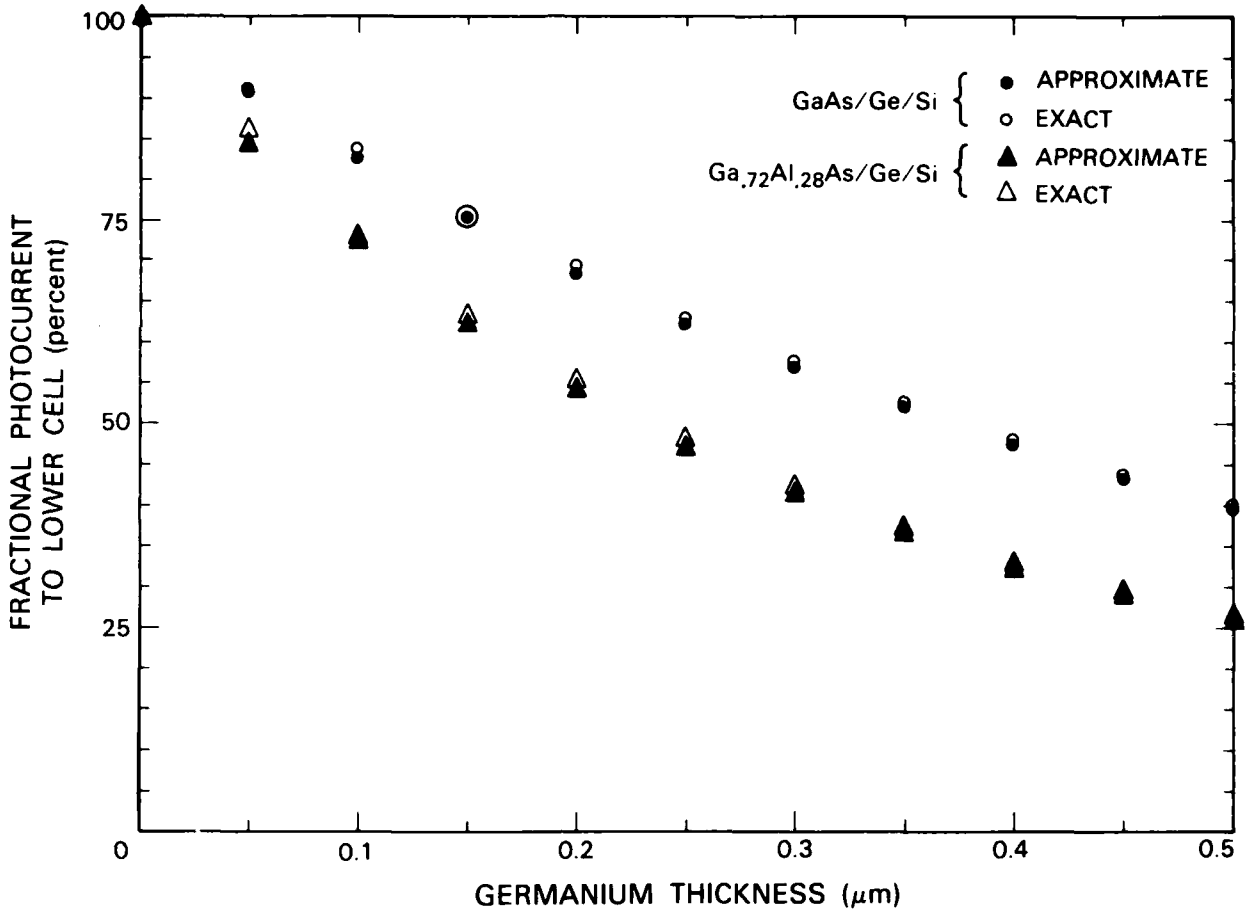

Figure 3-6. Fractional current to lower cell vs Ge thickness.

Because the photocurrent must be the same for both cells in a monolithic tandem structure, a given reduction in Si cell photocurrent would produce at least as large a relative reduction in the combined conversion efficiency of the tandem cell. The results of Figure 3-6 therefore show that even very thin layers of Ge will produce significant reductions in efficiency. For d of only 0.15 μm, for example, the reductions in Si photocurrent calculated from the exact T values are 26.3 and 38.3% for the GaAs/Ge/Si and $Ga_{0.72}Al_{0.28}As$/Ge/Si structures, respectively. Furthermore, these values represent only lower limits on the actual reductions, since the transmission calculations were based on the optical properties of high-quality single-crystal Ge, and any defects or disorder in the Ge layer would increase the optical losses.

G.W. Turner

REFERENCES

1. T.H. Windhorn, G.M. Metze, B-Y. Tsaur, and John C.C. Fan, Appl. Phys. Lett. **45**, 309 (1984).

2. G.A. Lincoln, M.W. Geis, S. Pang, and N.N. Efremow, J. Vac. Sci. Technol. B **1**, 1043 (1983).

3. J.A. Stratton, *Electromagnetic Theory* (McGraw-Hill, New York, 1941), p. 513.

4. MICROELECTRONICS

4.1 GaAs PERMEABLE BASE TRANSISTOR WITH 18.5-dB GAIN AT 18 GHz

About three years ago at this Laboratory, a particularly good wafer of permeable base transistors was fabricated using $AsCl_3$-GaAs-H_2 vapor phase epitaxy (VPE) for the GaAs overgrowth of the submicrometer tungsten base gratings. This wafer yielded a number of devices having an extrapolated maximum frequency of oscillation (f_{max}) of 100 GHz.[1] Numerous VPE-overgrown wafers have been fabricated in the years since then, but none of these devices has had an f_{max} exceeding 55 GHz. Recently, organometallic chemical vapor deposition (OMCVD) has been used instead of VPE for the overgrowth step, which has eliminated the incorporation of chlorine near the gratings during the overgrowth process.[2,3] Also, an extensive effort has been undertaken to reduce the levels of other undesired impurities incorporated in the overgrowth[4,5] using secondary ion mass spectrometry (SIMS) analysis for impurity identification. As a result, the average performance of recently fabricated devices has improved sharply, in spite of several undesired impurities which still remain. The best of these devices had a maximum stable gain of 18.5 dB at 18 GHz, which is the highest value yet obtained with a permeable base transistor.

A schematic of the PBT structure is shown in the cross section in Figure 4-1 and is essentially the same as that described earlier.[6] A dashed line indicates the critical interface between the first epitaxial layer grown by VPE and the second grown by the OMCVD layers. The doping concentration profile in the overgrown GaAs has been found to be an important factor in device

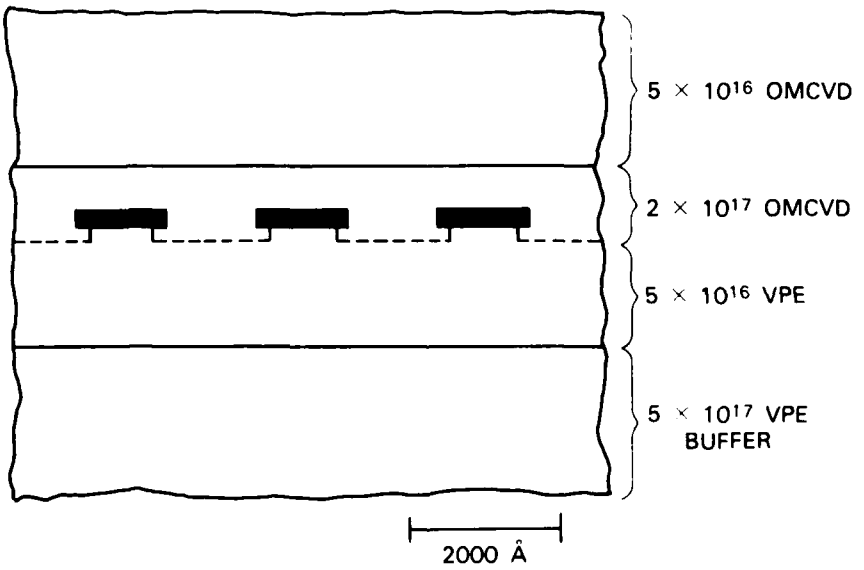

Figure 4-1. Cross-sectional view of a portion of the permeable base transistor indicating the carrier concentrations used. The dashed line indicates the interface between the first and second epitaxial layers.

performance. Wafers having flat profiles have had much lower collector currents and transconductances than predicted. It has been empirically observed that better performance is obtained when a higher concentration of 2×10^{17} cm^{-3} is used for the first 1000 Å of overgrowth and a concentration of 5×10^{16} cm^{-3} is used for the rest of the epitaxial film, as shown in Figure 4-1. The best devices made recently have a low-frequency transconductance of 75 mS/mm (as measured on a curve tracer) for a 2-mm equivalent gate-width device, a base-to-emitter threshold voltage of -0.6 V, and an output resistance above 150 Ω for collector voltages greater than 1 V. Network analyzer measurements of the scattering parameters yield the maximum stable power gain and short circuit current gain shown in Figure 4-2. The power gain at 18 GHz of 18.5 dB is slightly better than the result of three years ago, which is also shown in Figure 4-2 for comparison. The extrapolated f_{max} for the new device using a 6-dB/octave rolloff with frequency is 150 GHz. These results are comparable to those of the best GaAs MESFETs and HEMTs.[7,8] The value for f_T is approximately 35 GHz for the old and new devices. The measured scattering parameters have also been used to derive element values for the equivalent circuit of Figure 4-2. These values are R_B = 1.3 Ω, R_E = 1.3 Ω, R_O = 432 Ω, C_{BE} = 0.97 pF, C_{BC} = 0.015 pF, and g_m = 181 mS. A noise figure of 2.5-dB noise was measured with an associated gain of 13 dB at 10 GHz, which is not quite as good as the value of the earlier best result.[1] It is possible that the noise properties of the device are degraded by the unwanted impurities, as described below.

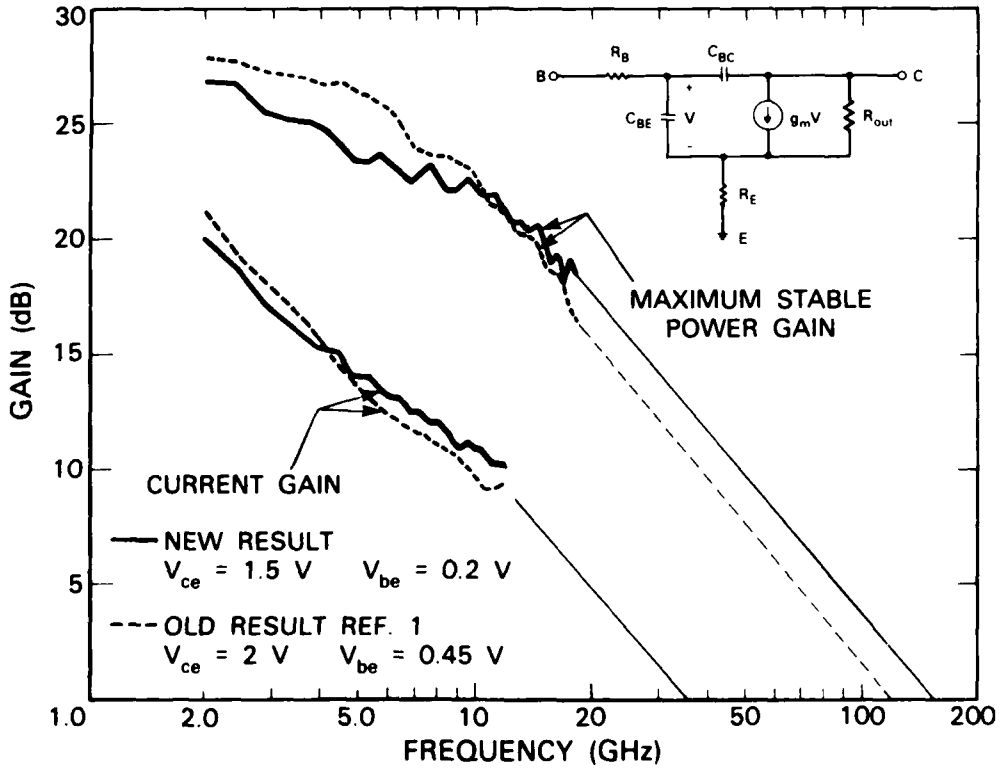

Figure 4-2. Maximum stable power gain and short circuit current gain for the recent best result compared with the old result. The extrapolations to the right are made using a roll-off of 6 dB/octave.

A detailed SIMS analysis of the materials in these devices has shown that there are many unintentional impurities such as sulfur, carbon, oxygen, gold, and copper in the grating region. Except for the sulfur, these impurities have much lower concentrations in areas of the wafer where there is no grating. It has been determined that the sulfur comes from a very slight residue of the hot sulfuric acid cleaning step. We have learned that our plasma asher introduced gold contamination and that our tungsten sputtering target[5] contains trace levels of carbon, oxygen, copper, and gold. The source of the oxygen and the carbon could also be the insufficient cleaning of the surface prior to epitaxial overgrowth. It should be possible to reduce all of these levels by using high purity tungsten and improving the processing techniques.

In order to better understand the location of the unwanted impurities in the grating region, a special procedure was designed using SIMS analysis.[5] This procedure was used for a SIMS profile of a specimen taken from the wafer of Figure 4-2. The result is given in Figure 4-3. The peaks in the center of Figure 4-3 are the impurity concentrations in the region of the grating, and the flat region to the left is the SIMS background level for each impurity. The profile shows the

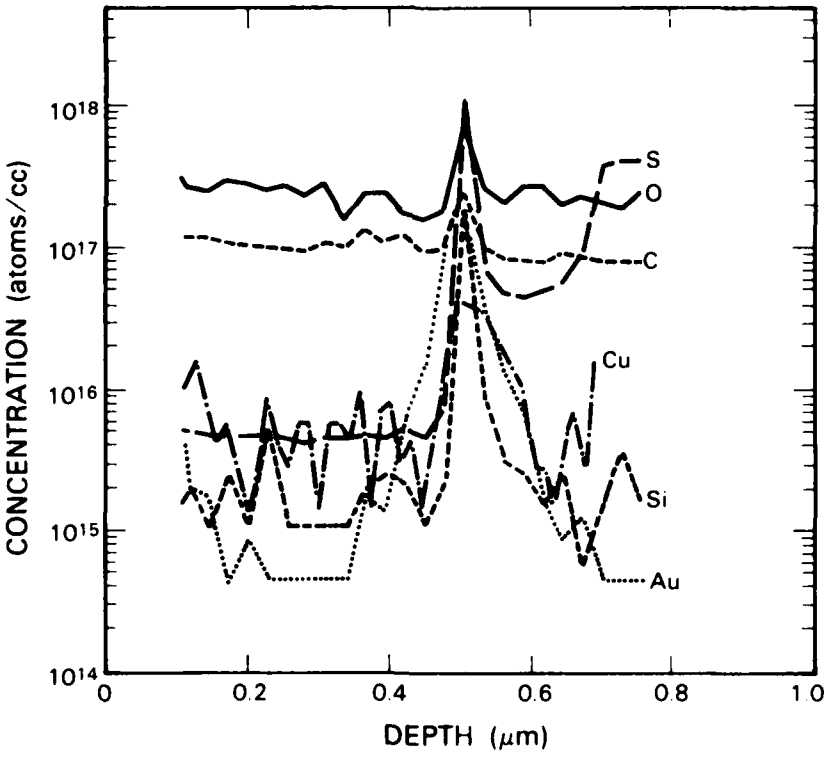

148456-N

Figure 4-3. SIMS profile of several elements in a specially prepared companion sample to the wafer in Figure 4-2. The peaks in the center indicate that a large concentration of unwanted impurities is incorporated in the GaAs in the vicinity of the grating region.

presence in the epitaxial overgrowth of silicon and sulfur, which are likely to be donors, and gold, copper, carbon, and oxygen, which are likely to be acceptors or traps. Gold and copper have been shown to diffuse from the W lines into the GaAs during overgrowth. Control experiments have shown that none of the impurities are residues from the etching.

It is likely that the sample on which the PBT fabrication was completed has similar impurity levels. These impurities can cause carrier compensation, making the carrier concentration profile difficult to control, and increase the scattering, which will lower the mobility and the electron velocity in the critical region of the device.

It has been predicted that electrons in the PBTs should exhibit average velocities as high as four times the saturated drift velocity.[6,9] This high velocity would produce a g_m for the device of Figure 4-3 of 600-1000 mS (300-500 mS/mm), an f_t of 80-160 GHz, and an f_{max} above 200 GHz. However, the results of Figure 4-2 and the derived equivalent circuit parameters are in approximate agreement with performance predicted by an average electron velocity of 1×10^7 cm/s (Reference 6). It is possible that the scattering from the large number of unwanted impurities in these devices is limiting the electron velocity to this lower value. The scattering and charge trapping in these devices may also be the primary source of noise. We believe that it may be possible to reach the frequencies predicted from the higher velocities by reducing the unwanted impurities.

C.O. Bozler
M.A. Hollis
K.B. Nichols
S. Rabe
A. Vera
C.L. Chen

4.2 ROOM-TEMPERATURE NEGATIVE RESISTANCE AND OSCILLATIONS IN RESONANT TUNNELING STRUCTURES

We have recently observed room-temperature negative differential resistance from double-barrier resonant tunneling structures similar to those described earlier.[10] Figure 4-4 shows I-V curves from one device taken at both 300 and 20 K. The high peak current densities have been maintained (10^4 A/cm^2), so that the negative impedance levels for 3 μm devices were on the order of 100 ohms. This fact made it difficult to quench the oscillations in the negative differential resistance region, and the discontinuities in the I-V curve are a result of these oscillations. Spectrum analyzer measurements showed that power of about 1 μW was produced in sharp lines at fundamental frequencies up to 20 GHz. The frequency limit in this case was set by the coaxial circuit. The maximum output power expected from calculations based on the I-V curve[10] are in approximate agreement with the observations.

The reason that earlier samples did not show negative differential resistance at room temperature is not completely understood. There is some evidence that previously the resonant part of the I-V curves was being swamped by a temperature-dependent leakage current, perhaps due to tunneling via impurity or trap levels in the AlGaAs barriers. The molecular beam epitaxy growth chamber was particularly clean when the current samples were grown, so it is presumed that the

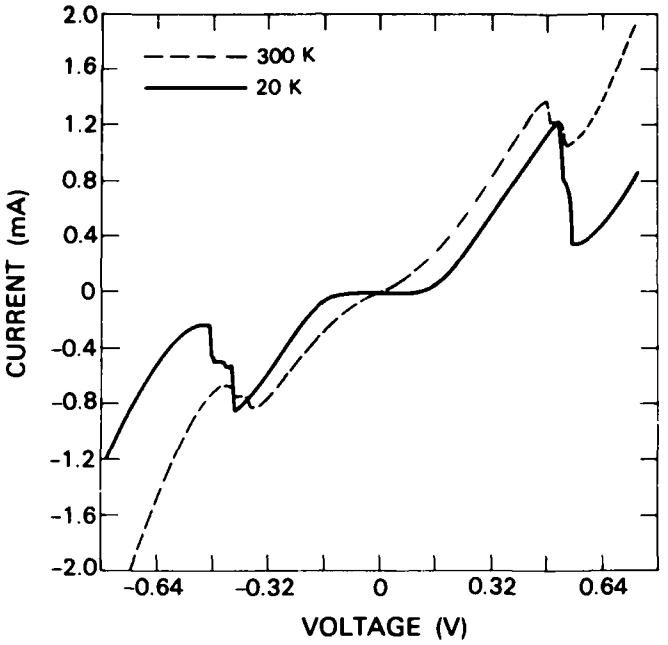

149441-N

Figure 4-4. Current-voltage curves of resonant tunneling structure showing negative differential resistance at room temperature as well as 20 K.

impurity levels were very low. Since then, six additional wafers have been grown and all show room-temperature negative differential resistance.

T.C.L.G. Sollner
P.E. Tannenwald
W.D. Goodhue

4.3 RECENT ADVANCES IN SOI FILMS PRODUCED BY ZONE-MELTING RECRYSTALLIZATION

Subboundaries have been consistently observed in films of AgCl, (Reference 11) Ge, (Reference 12) salol, (Reference 13) InSb[14,15] and Si[16-19] produced by zone-melting recrystallization (ZMR). The present study of subbboundaries in Si was concentrated on the two basic structures shown in Figure 4-5. When subjected to ZMR in a graphite-strip-heater oven with improved thermal characteristics,[20] these structures gave different subboundary morphologies, as shown in Figure 4-6 by optical micrographs of the etched surface of two films. The thinner Si films [Figure 4-5(b)] contained branched subboundaries [Figure 4-6(a)], while the thicker Si films with a thicker lower oxide [Figure 4-5(a)] contained a lower density of subboundaries, without branching,[21,22] as shown in Figure 4-6(b). Figure 4-6(b) also shows several locations where a series of tangled dislocation clusters forms a linear array, with defect-free material between the successive clusters.

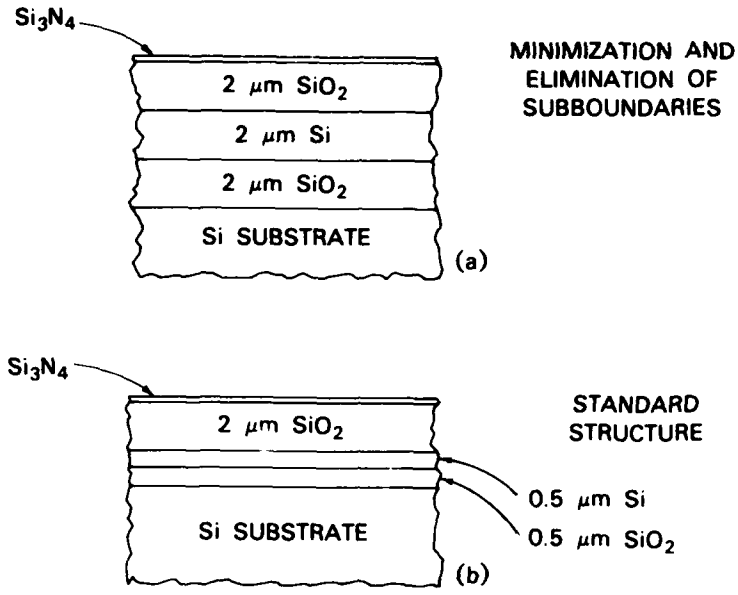

144847-N-01

Figure 4-5. Two basic structures of zone-melting recrystallization (ZMR) of Si films.

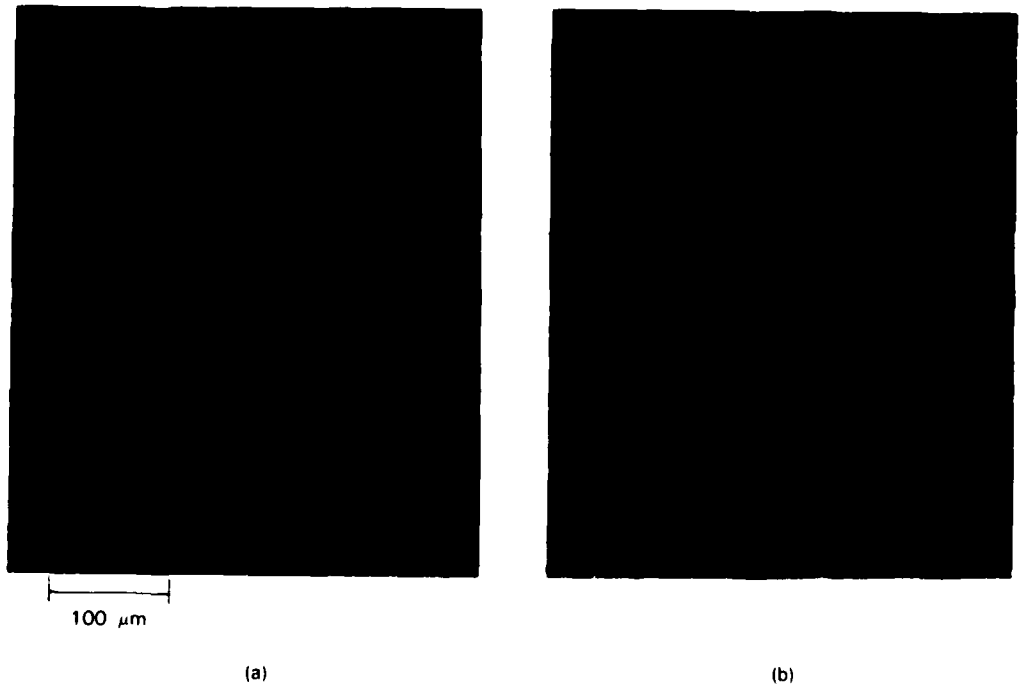

135070-R-02

Figure 4-6. Optical micrographs of the etched surfaces of two ZMR Si films. (a) The Si and SiO_2 films were 0.5 μm thick, as depicted in Figure 4-5(b). (b) the Si and SiO_2 films were 2 μm thick, as depicted in Figure 4-5(a).

The angular discontinuities across the subboundaries present in ZMR Si films associated with the two structures of Figure 4-5 were markedly different. Figure 4-7 shows a comparison of the angular discontinuity across subbboundaries for the thin and thick film cases as determined by transmission electron microscope. The structure with thicker Si and SiO_2 exhibits substantially smaller angular discontinuities than the thinner structure.

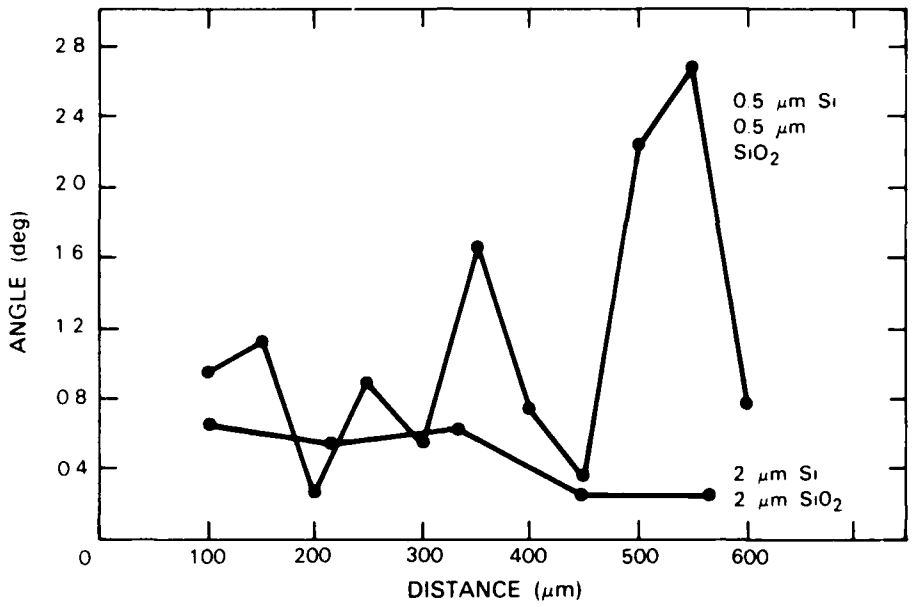

144844-N.A

Figure 4-7. Comparison of the angular discontinuity across the subboundaries.

The thicker ZMR films are less defective than the thin films. Often there are linear arrays of regularly spaced dislocation clusters between which the material is nearly defect-free. In other locations there are narrow bands of random dislocations. When these thicker films are annealed for 8 hours at 1250°C in an oxidizing atmosphere, nearly defect-free material is often obtained with only a few isolated dislocations.[23] Optical micrographs of such a film, which was chemically etched to reveal defects, shows that a large area of the film is free of any visible defects. Figure 4-8 shows TEM micrographs of a 0.5-μm-thick ZMR Si film and a 2-μm-thick recrystallized and annealed film. The thinner film contains many obvious subboundaries while the thicker film contains only an occasional dislocation over an area of a few square millimeters.

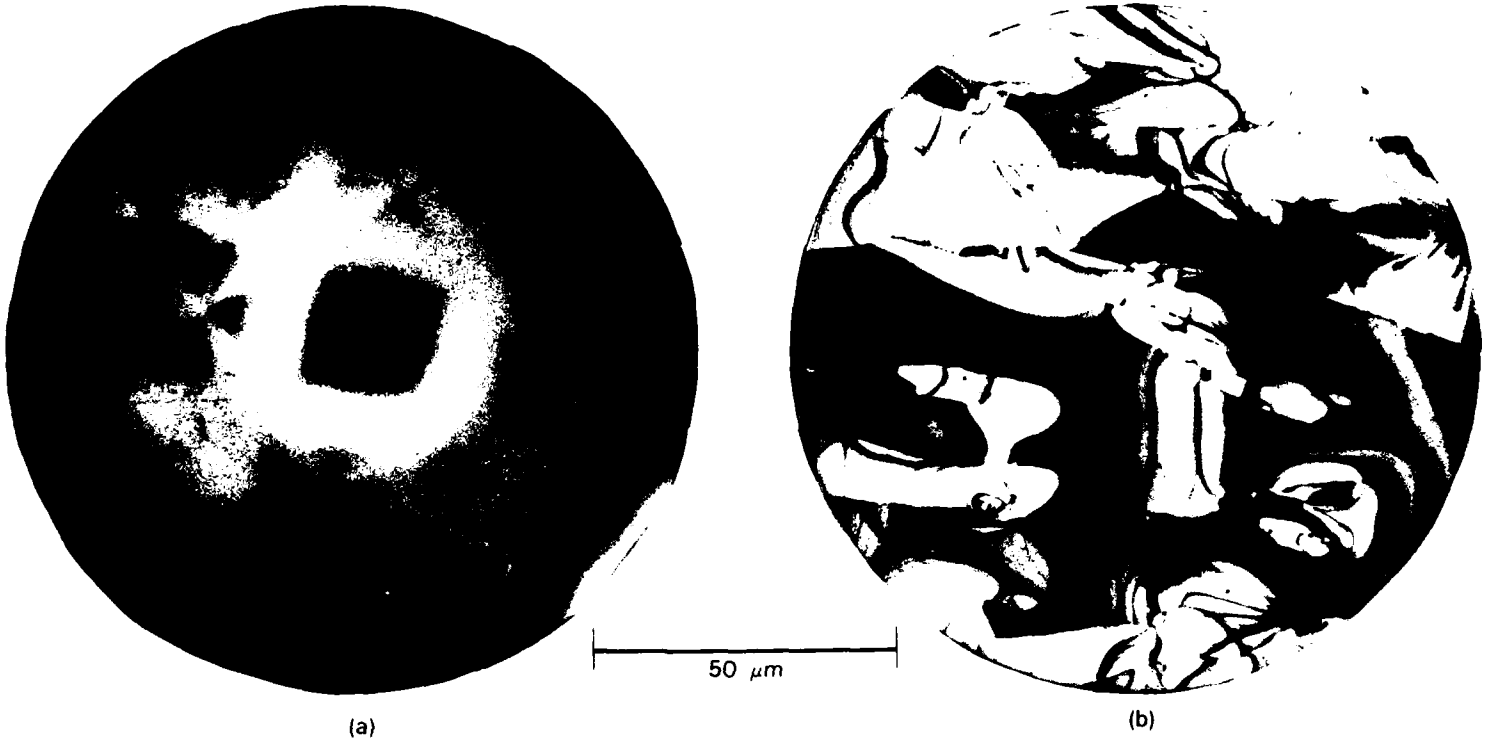

Figure 4-8. Transmission electron micrographs of two ZMR Si films. (a) Micrograph obtained from an annealed and chemically thinned 2-μm-thick film. (b) Micrograph obtained from a 0.5-μm-thick film.

Several authors[24-27] have discussed cellular growth due to constitutional supercooling as a cause of subboundaries in ZMR films, so only a brief discussion will be given here. Table 4-1 lists the impurities commonly present in graphite-strip-heater recrystallized Si films, their atomic fractions estimated from secondary ion mass spectrometry[28] and their segregation coefficients.[29] The thermal gradient, G, necessary to stabilize the liquid-solid interface against cellular growth is given by the equation[30]

$$G = C\ R\ m\ (1-k)\ /\ (D\ k),$$

where C is the atomic fraction of the impurity, R is the speed of solidification, m is the liquidus slope, k is the segregation coefficient, and D is the diffusion coefficient[29] of the dopant in liquid Si (assumed to be 3×10^{-4} cm^2-s^{-1}). The values of G calculated from this expression for the impurities in Si and ZMR speeds of 1 and 0.1 mm s^{-1}, are listed in Table 4-1. For the more commonly used ZMR speed of 1 mm-s^{-1}, G is the order of 100 K cm^{-1}, which is within an order of magnitude of the estimated thermal gradient.[31] For ZMR speeds in excess of 1 mm s^{-1}, or for higher impurity concentrations than those listed in Table 4-1, constitutional supercooling may be a factor in subboundary formation. The ZMR speeds used in the work reported here varied from 0.1 to 0.2 mm-s^{-1}. For these speeds, the calculated value of G is about 10 K cm^{-1}, which is much less than the estimated gradient. Hence, it is unlikely that constitutional supercooling is a factor in the present work.

In summary, we have measured the dependence on film thickness of the angular discontinuities across subboundaries in ZMR Si films. Thicker ZMR films are less defective than thinner films. The defects often can be eliminated from large areas by annealing in O_2 for several hours in the thick film case. At the scanning rates used in these experiments cellular growth due to constitutional supercooling is unlikely. Deformation due to stress induced by thermal gradients and expansion on freezing may give rise to subboundaries.

M.W. Geis
C.K. Chen
H.I. Smith
R.W. Mountain
C.L. Doherty

TABLE 4-1

Properties of Impurities in Molten Si

Impurity	Atomic fraction C	Segregation coefficient k	Liquidus slope m (degrees per atomic fraction)	Thermal Gradient G ($K\ cm^{-1}$)	
				for R = 1 mmx sec^{-1}	for R = 0.1 mmx sec^{-1}
O	2 to 4×10^{-5}	0.3-1.20	420	6.7	0.67
Cu	2×10^{-7}	4×10^{-4}	600	96	9.6
C	2×10^{-5}	6×10^{-2}	520	62	6.2
N	2×10^{-8}	7×10^{-4}	600	56	5.6

4.4 PLASMA-ETCHED VIA HOLES FOR GaAs FETs

The use of via transistors has become an important part of the technology development for producing GaAs monolithic microwave integrated circuits (MMICs). The advantages of via transistors are higher gain, wider bandwidth, and increased packing density compared to wire bonded devices, especially for frequencies above 4 GHz. We have developed a highly versatile plasma mode dry etching process for producing 3-4 mil deep via holes in GaAs using CCl_2F_2 plus small additions of N_2 or O_2. This process combined with the electroless plating of Pd was used to make source via connections for 1.5 μm channel length GaAs MESFETs. These devices exhibited nearly 4 dB maximum available gain at 16 GHz.

Plasma-etched via connections to GaAs FETs were first demonstrated by D'Asaro et al.[32] using BCl_3-Cl mixtures in a high pressure ($>$ 150 mTorr) plasma, but in a "quasi" RIE mode in that the wafers were mounted on the RF driven electrode. By adjusting the Cl_2 concentration in the feed gas mixture they were able to control the degree of etching anisotropy, but etch rates were less than 0.4 μm/min. Recently Hipwood and Wood[33] demonstrated a via hole process using CCl_2F_2 under nearly identical conditions as D'Asaro. Etch rates were substantially higher (2-3 μm/min), but usable profiles were accompanied by etch depth nonuniformities and polymer formations.

We found that the addition of small amounts of O_2 or N_2 to a CCl_2F_2 plasma results in a versatile GaAs etching process. The wafers were placed on the grounded electrode of a conventional parallel plate reactor driven at 13.56 MHz with a power density of 1.3 W/cm^2 at a total system pressure of 200 mTorr. In contrast to the "quasi" RIE mode of the aforementioned results, the substrates were subjected to little or no ion bombardment, as was evident by the low self-bias ($<$ 5 V). The etch rate dependence of O_2 and N_2 additions to the CCl_2F_2 feed gas are shown in Figure 4-9, where total gas pressure was kept constant to 200 mTorr. For O_2 or N_2 concentrations up to 15% of total gas pressure, orientation dependent etching resulted, with an etch rate as high as 9 μm/min. being obtained for a 5% O_2-CCl_2F_2 mixture. This high etch rate had been observed previously only for pure Br_2 and Cl_2 plasma discharges.[34] For N_2 and O_2 concentrations greater than 15%, etch rates were reduced ($<$ 2 μm/min) and orientation dependence was diminished. The decrease in etch rates was balanced by an increase in the degree of anisotropy (the vertical to horizontal etch rate ratio). Details about the trade-offs between anisotropy and etch rates will be presented in future reports. A 10% N_2-CCl_2F_2 mixture was used to etch the via hole shown in Figure 4-10.

For the FET fabrication, a 2-μm undoped buffer layer and a 0.3-μm-thick active layer (1×10^{17} cm^{-3}) were grown sequentially by MBE on a semi-insulating substrate. FETs having a gate width of 500 μm and a gate length of 1.5 μm were fabricated. Source and drain ohmic contracts were alloyed Ni/Ge/Au. The gate was defined by optical lithography, and conventional lift off was used for the Ti/Au gate metal. After the device fabrication, the wafer was thinned to 5 mils by chemical etching. Via holes were then defined by back to front alignment. Plasma etching, as described above, was then used to etch the via holes. After stripping the Ni mask, a thin layer of Pd was electroless-plated to the backside of the wafer. A thick Au layer was plated for the ground plane and additional mechanical support. A completed device is shown in Figure 4-11.

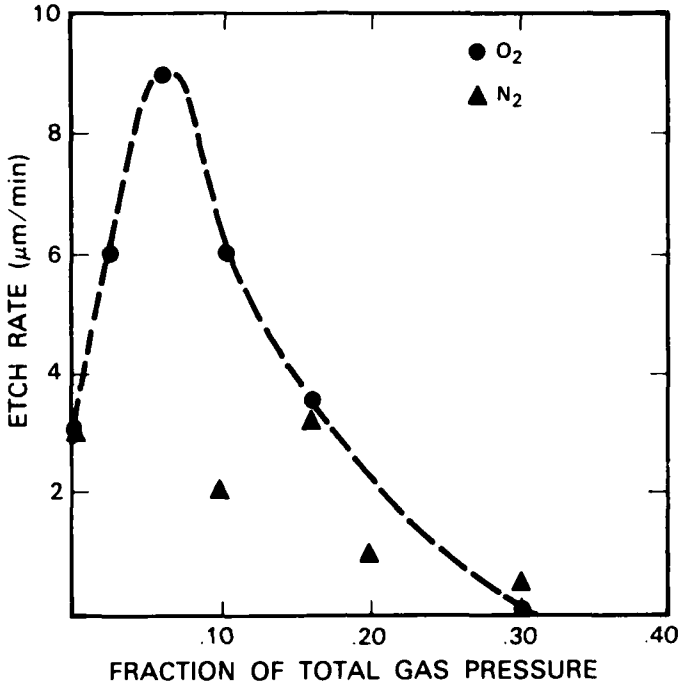

163904-N

Figure 4-9. The effects of O_2 or N_2 additions to CCl_2F_2 on GaAs etch rate.

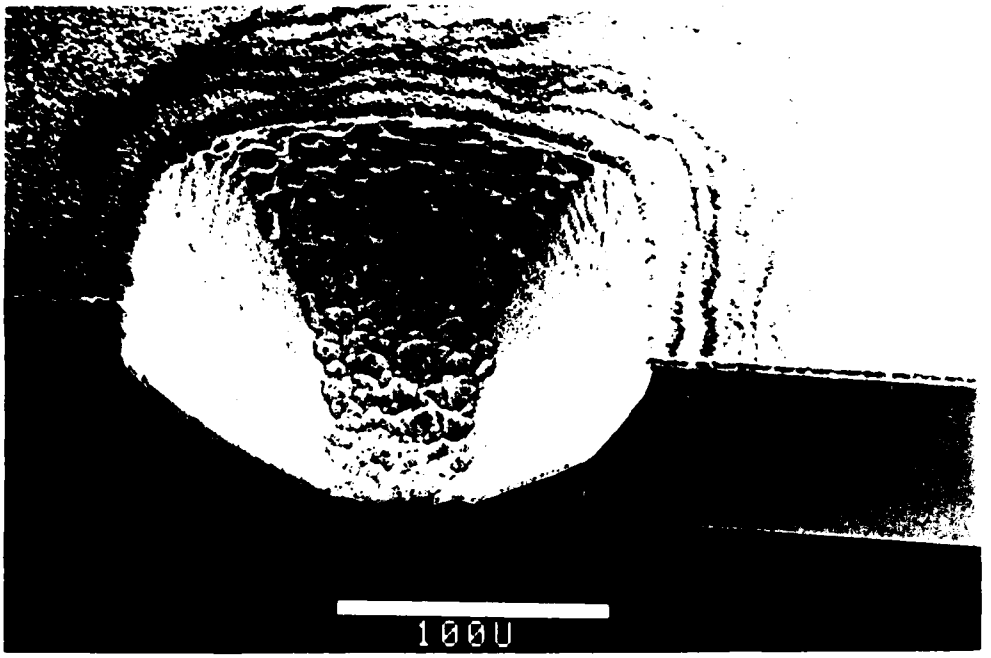

156573-N

Figure 4-10. SEM of a 4-mil-deep via hole etched in GaAs using a CCl_2F_2 mixture. A thick layer of Pd has been deposited by electroless plating.

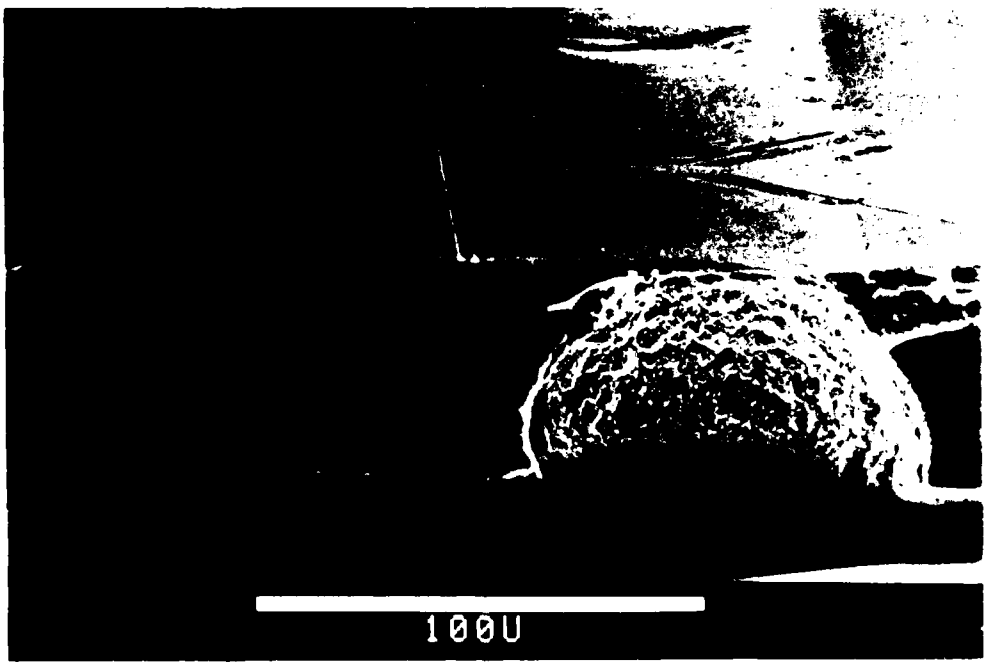

153906-N

Figure 4-11. SEM of completed GaAs MESFET cleaved through the via hole connection to the source pad.

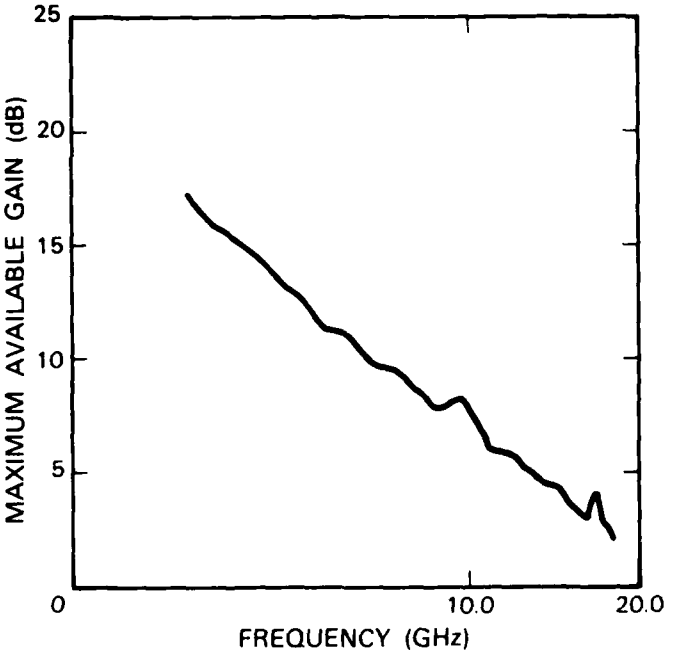

163906-N

Figure 4-12. Maximum available gain vs frequency obtained for a 1.5 μm length GaAs MESFET which incorporated the via hole technology.

The MESFET exhibited 90 mA saturation current at zero gate bias, with a 3-V pinch-off voltage. The transconductance was 80 mS/mm. The device had a maximum frequency of oscillation of 25 GHz and exhibited a maximum available gain of 3.5 dB at 16 GHz as shown in Figure 4-12. These results demonstrate that a viable via hole process has been developed which should greatly enhance our ability to produce GaAs MMICs.

A.R. Forte
D.D. Rathman
L.J. Mahoney
C.L. Chen

REFERENCES

1. Gary D. Alley et al., IEEE Trans. Electron Dev. **ED-29**, 1708 (Oct. 1983).
2. K.B. Nichols, R.P. Gale, M.A. Hollis, G.A. Lincoln, and C.O. Bozler, IEEE Trans. Electron Dev. **Ed-31**, 1969 (Dec. 1984).
3. H. Asai, S. Adachi, S. Audo, and K. Oe, J. Appl. Phys. **55**, 3868 (May 1984).
4. M.A. Hollis, K.B. Nichols, C.O. Bozler, A.R. Calawa, and M.J. Manfra, Program of the 1984 Electronic Materials Conf., Univ. of Calif., Santa Barbara, CA, June 20-22, Metallurgical Society of AIME.
5. M.A. Hollis, K.B. Nichols, and C.O. Bozler, to be published.
6. C.O. Bozler, G.D. Alley, IEEE Trans. Electron Dev. **ED-27**, 1128 (June 1980), DTIC AD-A096619.
7. U.K. Mishra, S.C. Palmateer, P.C. Chao, P.M. Smith, and J.C.M. Hwang, IEEE Electron Dev. Lett. **EDL-6**, 142 (March 1985).
8. M. Feng, V.K. Eu, T. Zieliuski, H. Kanber, and W.B. Henderson, IEEE Electron Dev. Lett. **EDL-5**, 18 (Jan. 1984).
9. Y. Awano, K. Tomizawa, and N. Hashizume, to be published in 11th Int. Symp. on Gallium Arsenide and Related Compounds (Biarritz, France) The Institute of Physics. (Sept. 1984).
10. T.C.L.G. Sollner, P.E. Tannenwald, D.D. Peck, and W.D. Goodhue, Appl. Phys. Lett. **45**, 1319-1321 (1984), DTIC-AD-A150698.
11. J.M. Hedges and J.W. Mitchell, Phil. Mag. A **44**, 223 (1953), and J.W. Mitchell, Proc. R. Soc. London A **371**, 49 (1980).
12. J. Maserjian, Solid-State Electron. **6**, 477 (1963).
13. K.A. Jackson and C.E. Miller, J. Crystal Growth **42**, 364 (1977).
14. A.R. Billings, J. Vac. Sci. Technol. **4**, 757 (1969).
15. C.C. Wong, C.J. Keavney, H.A. Atwater, C.V. Thompson, and H.I. Smith, in *Energy Beam-Solid Interactions and Transient Thermal Processing*, J.C.C. Fan and N.M. Johnson, eds. (Elsevier, North Holland, New York, 1984), 627.
16. T.O. Sedgwick, R.H. Geiss, S.W. Depp, V.E. Hanchett, B.G. Huth, V. Graf, and V.J. Silvestri, J. Electrochem. Soc. **129**, 2802 (1982).
17. M.W. Geis, H.I. Smith, B-y. Tsaur, J.C.C. Fan, D.J. Silversmith, and R.W. Mountain, J. Electrochem. Soc. **129**, 2812 (1982).

18. M.W. Geis, H.I. Smith, D.J. Silversmith, R.W. Mountain, and C.V. Thompson, J. Electrochem. Soc. **130**, 1178 (1983).

19. J.R. Davis, R.A. McMahon, and H. Ahmed, in *Laser-Solid Interactions and Transient Thermal Processing of Materials*, J. Narayan, W.L. Brown, and R.A. Lemons, eds. (Elsevier, North Holland, New York, 1983), 563.

20. C.K. Chen, M.W. Geis, H.K. Choi, B-Y. Tsaur, and J.C.C. Fan, in *Energy Beam-Solid Interactions and Transient Thermal Processing*, D.K. Biegelsen, G.A. Rozgonyi, and C.V. Shank, eds. (Materials Research Society, 1985).

21. L. Pfeiffer, T. Kovacs, and K.W. West, in *Energy Beam-Solid Interactions and Transient Thermal Processing*, D.K. Biegelsen, G.A. Rozgonyi and C.V. Shank, eds. (Materials Research Society, 1985).

22. H.A. Atwater, H.I. Smith, C.V. Thompson, and M.W. Geis, Mater. Lett. **2**, 269 (1984).

23. L. Pfeiffer and co-workers have also demonstrated the removal of isolated defects in ZMR Si films by annealing (personal communication).

24. H.J. Leamy, C.C. Chang, H. Baumgart, R.A. Lemons, and J. Cheng, Mater. Lett. **1**, 33 (1982).

25. R.A. Lemons, M.A. Bosh, and D. Herbst, in *Laser-Solid Interactions and Transient Thermal Processing of Materials*, J. Narayan, W.L. Brown, and R.A. Lemons, eds. (Elsevier, North Holland, New York, 1983), 581.

26. E-H. Lee, in *Energy Beams-Solid Interactions and Transient Thermal Processing*, D.K. Biegelsen, G.A. Rozgonyi, and C.V. Shank, eds. (Materials Research Society, 1985).

27. J.C.C. Fan, B-Y. Tsaur, C.K. Chen, J.R. Dick, and L.L. Kazmerski, Appl. Phys. Lett. **44**, 1086 (1984).

28. R.F. Pinizzotto, F.Y. Clark, S.D.S. Malhi, and R.R. Shah, in *Comparison of Thin Film Transistors and SOI Technology*, H.W. Lam, ed. (Elsevier, North Holland, New York, 1984).

29. W. Zulehner and D. Huber, in *Crystals: Growth, Properties and Applications Vol. 8*, H.C. Freyhardt, ed. (Springer-Verlag, New York, 1982), 1-143.

30. J.D. Verhoeven, *Fundamentals of Physical Metallurgy* (John Wiley and Sons, New York, 1975).

31. H.E. Cline, J. Appl. Phys. **54**, 2683 (1983).

32. L.A. D'Asaro, A.D. Butherus, J.V. DiLorenzo, D.E. Iglesias, S.H. Wemple, in *Gallium Arsenide and Related Compounds*, H.W. Thin, ed., (The Institute of Physics, London 1980) 267-73.

33. L.G. Hipwood and P.N. Wood, J. Vac. Sci. Tech. B 3[1] 395 (1985).

34. V.M. Donnely, D.J. Flamm, C.W. Tu, and D.E. Ibbotson, J. Chem. Soc. **129**, 2533 (1983).

5. ANALOG DEVICE TECHNOLOGY

5.1 RF LOSSES OF HIGH-TRANSITION-TEMPERATURE SUPERCONDUCTORS

If superconductive signal processing devices are to attain widespread application, they must be operable with closed-cycle cryocoolers. Because the efficiency of small cryocoolers decreases dramatically[1] when the necessary temperature drops below 10 K, we are investigating the use of high-T_c materials to implement these processors. Superconductive analog devices use long electromagnetic delay lines as one of their principal elements. Evaluation of conductor losses for these lines is imperative. We have extended our earlier resonator measurements[2] to allow the evaluation of losses in superconductors between 4.2 K and 25 K and in the frequency range of 200 MHz to 18 GHz. Our initial results indicate that, contrary to conventional wisdom, the microwave losses of Nb and NbN are acceptably low at temperatures within 1-2 K of their transition temperatures T_c.

The loss in a transmission line can be easily evaluated by the use of a capacitively coupled resonator, as shown schematically in Figure 5-1. This resonator can be fabricated in a stripline configuration by forming gaps in both ends of the line. The capacitance between the two sides of the gap provides input and output coupling. Resonance occurs at frequencies at which the transmission line is an integral number of half-wavelengths long. The line loss α can be determined from the width and height of the resonant transmission peak.

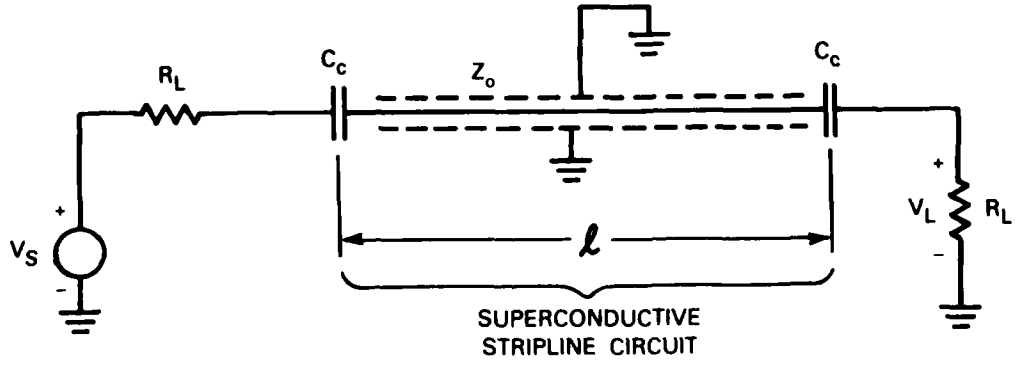

153907-N

Figure 5-1. Schematic of the transmission measurement of a gap-coupled stripline resonator.

Generally, the loss constant α is the sum of the conductor loss $\alpha_c = R/2Z_o$, where R is the transmission-line series resistance per unit length, and the dielectric loss. R is proportional to the superconductor's surface resistance R_s. In our measurements, the resonator geometry and dielectric loss tangents are such that the conductor losses dominate, except at the lowest frequencies and temperatures.

The two-fluid model predicts a temperature-dependent surface resistance of the form

$$R_s = R_o (f/f_o)^2 (T/T_c)^4 [1 - (T/T_c)^4]^{-3/2} \quad (1)$$

where R_o and f_o are constants.[3] The more exact Mattis-Bardeen analysis[4] offers no accurate closed-form expression for $T > T_c/2$; for $T < T_c/2$, a surface resistance of the form[5]

$$R_s = R_1 (f/f_o)^{1.7} \exp\left(-\frac{\Delta_o T_c}{T}\right) \quad (2)$$

is predicted, in which f_o and R_1 are constants and $\Delta_o \approx 2$ is the reduced energy gap. In practice an additive temperature-independent term R_{res} has to be added to expressions (1) and (2) to account for other residual losses not covered by the theories. R_{res}, in general, will be very dependent on the deposition conditions of the superconductor. Our measurements indicate surface resistances which are more weakly dependent on temperature than predicted by either Equation (1) or (2), especially as T_c is approached. It is possible that R_{res} dominates.

Experimental results using 2-in. substrates have been described before.[2] More recently, we have been using resonators of different superconducting materials deposited on Tyco Saphikon c-axis-in-plane ribbon-grown sapphire substrates. The high temperatures used for deposition of many of these alloy superconductors exclude the use of silicon. The substrates are 0.5 × 12.5 × 25 mm. A typical pattern is shown in Figure 5-2. Generally, three films are necessary. Most deposition systems require clamping the substrate to a heater block, thus precluding the deposition of films on both sides of the substrate. The package configuration is shown in Figure 5-3. Careful grounding is essential for the prevention of feedthrough from the input to output lines, which can bypass the weakly coupled resonator and obscure the resonant peaks. The whole structure is clamped by a bed of springs; rigid clamping of the substrates is necessary to reduce microphonics which can cause jitter in the resonant frequencies.

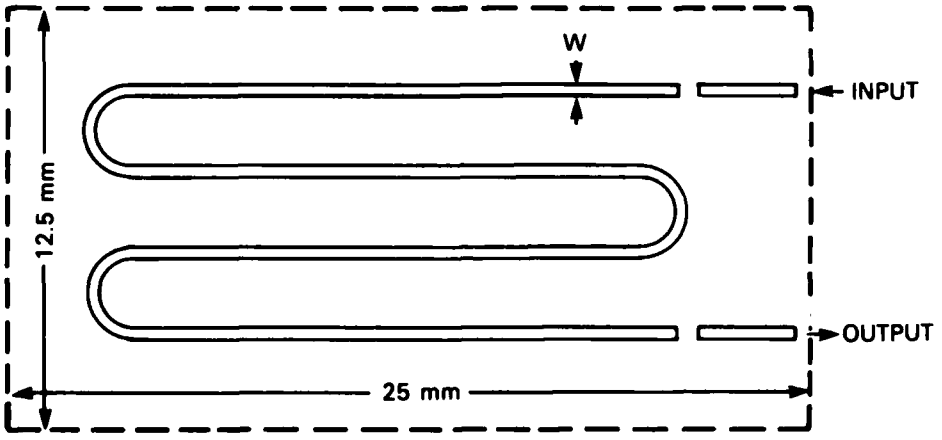

Figure 5-2. Photolithographic pattern of a thin-film superconductive stripline resonator.

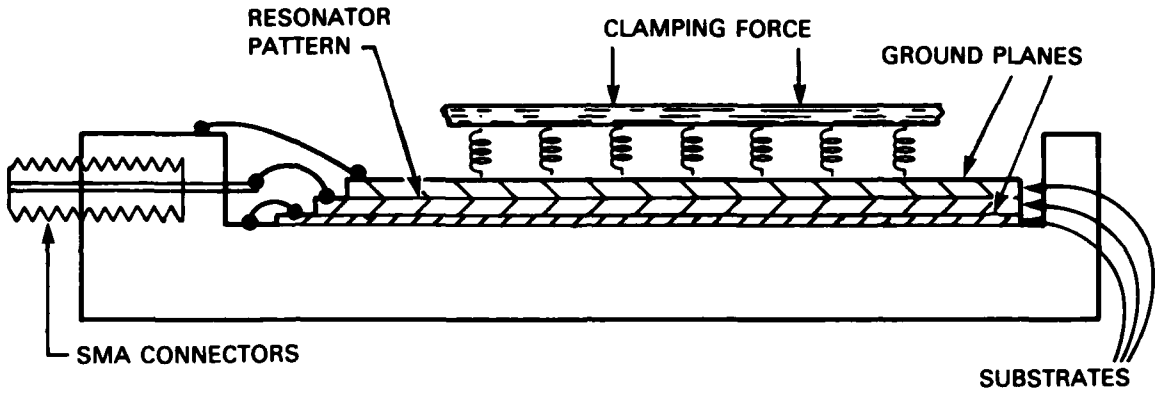

153909-N

Figure 5-3. Superconducting resonator package.

The measurements are made using an automatic vector network analyzer. The temperature of the resonator is controlled by a programmable temperature controller and does not change by more than 50 mK during a frequency scan.

A typical result for 4000-Å-thick Nb films is shown in Figure 5-4. The films used for the measurements in Figure 5-4 were deposited on unheated substrates by RF diode sputtering. These

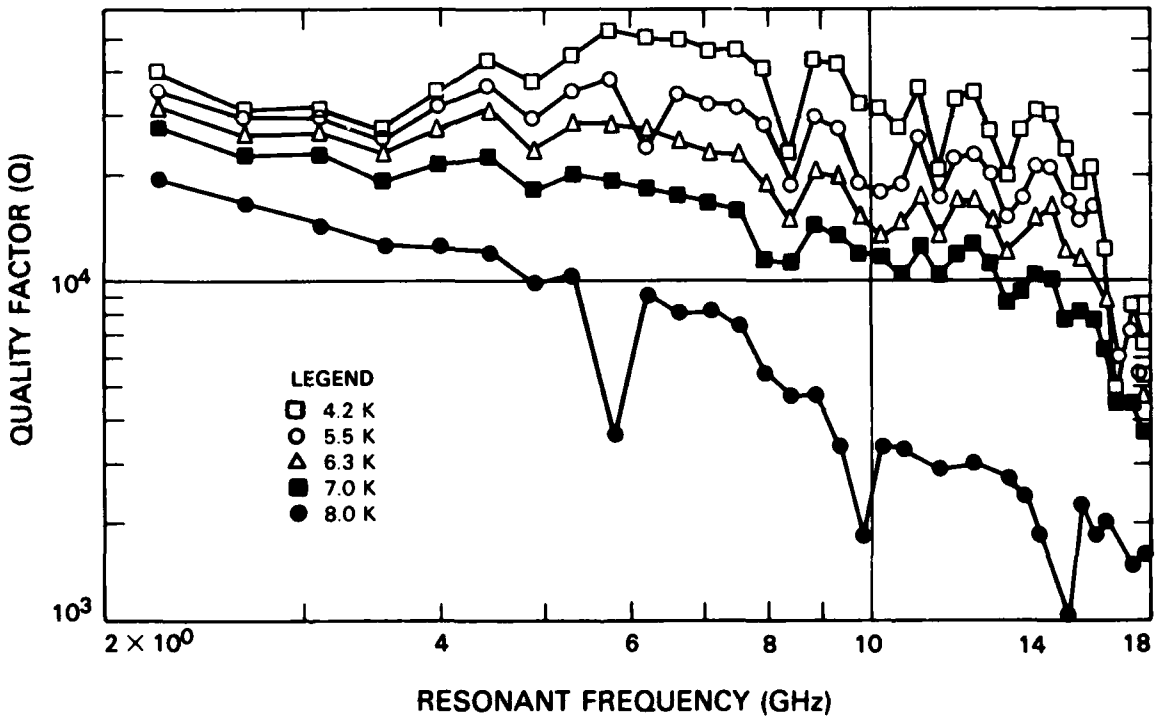

153910-N

Figure 5-4. Measured quality factors of a 50-ohm resonator based on 4000-Å-thick sputtered niobium films as a function of frequency, with temperature as a parameter. The substrates are 500-μm-thick sapphire.

films have a transition temperature of 9.0 K and are polycrystalline. In Figure 5-5 we have replotted the data of Figure 5-4 for just two frequencies as a function of $1/T$. In the same figure, we also show the data for two other films: (1) 2500-Å-thick Nb deposited by evaporation in ultra-high vacuum onto a 800°C substrate[6] and (2) 1.5-μm-thick NbN (or, more precisely, NbC_xN_y) films deposited by reactive sputtering onto 600°C substrates.[7] The latter films were

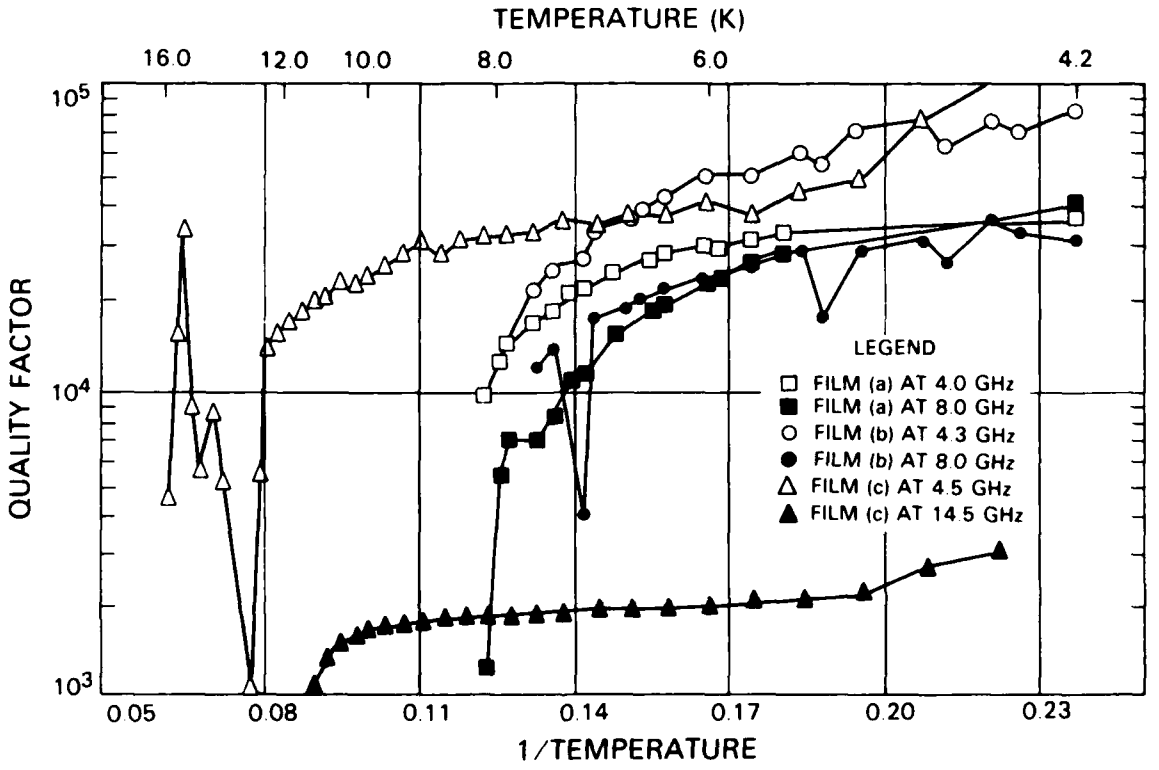

Figure 5-5. Measured quality factors, as a function of reciprocal temperature, of 50-Ω resonators based on: (a) 4000-Å-thick sputtered niobium on 500-μm-thick sapphire; (b) 2500-Å-thick evaporated niobium on 500-μm thick sapphire; and (c) 1.5-μm-thick reactively sputtered niobium nitride films on 125-μm-thick sapphire. Near T_c, the penetration depth becomes a very sensitive function of temperature. Temperature fluctuations consequently cause large changes in resonant frequencies and render linewidth measurements inaccurate.

deposited on 125-μm-thick Crystal Systems c-axis-normal sapphire. The results for NbN are particularly interesting since they indicate that devices with a TB product of more than 1000 at 4 GHz can be operated at temperatures compatible with existing closed cycle cryocoolers. These films are not deposited under clean room conditions and, invariably, are full of pinholes. The resulting nonuniformity in the resonator measurements makes any further conclusion at this time premature.

In the future we will extend these measurements to niobium nitride films deposited at lower substrate temperatures. Even the results obtained to date, however, indicate that wide-bandwidth superconductive signal-processing devices can be operated at temperatures above 10 K.

A.C. Anderson
R.S. Withers
G.L. Fitch

5.2 STACKED SUPERCONDUCTIVE DISPERSIVE DELAY LINES

Superconductive dispersive delay lines are being developed for use in multigigahertz-bandwidth analog signal-processing systems. The dispersive delay lines with greater than 2-GHz bandwidth previously reported[8] use a patterned niobium film deposited on a silicon substrate. With an additional silicon substrate as a cover, the patterned film is clad by symmetric silicon dielectric layers, each having a niobium ground plane (Figure 5-6). This stripline structure consists of two lines which are coupled by integral backward-wave couplers. The total dispersive delay achievable with this structure is limited to the maximum stripline length that can be accommodated on the single silicon wafer. This maximum length is constrained primarily by the maintenance of adequate isolation between adjacent turns of the delay line (which are wound in a spiral configuration). For practical, low-distortion stripline circuits on silicon, this translates to the requirement that the line spacing be no closer than 3.5 times the wafer thickness. For 125-μm-thick, 5-cm-dia. silicon substrates, the maximum dispersive delay of 38 ns has been achieved; for 7.5-cm-dia. Si, 96 ns should be achieved. An appropriate goal for analog signal processors is a time-bandwidth (TB) product of 1000, requiring delays of up to 500 ns.

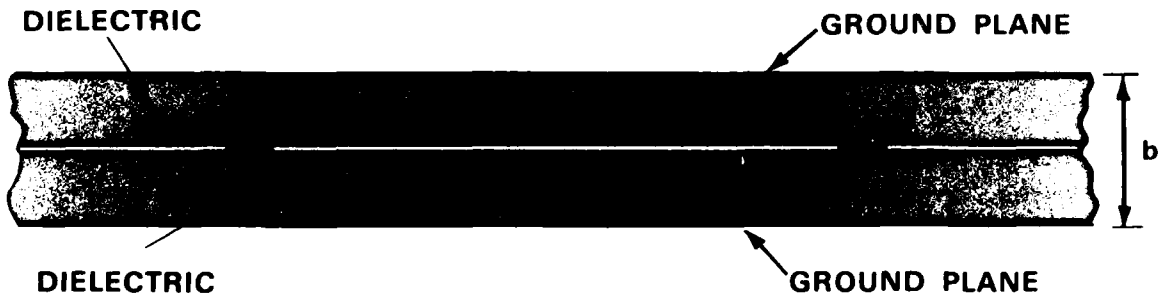

Figure 5-6. Stripline cross section.

We have recently developed a new, stacked superconductive dispersive delay line which has an increased electrical line length and a corresponding increase in potential signal-processing power. This structure (Figure 5-7) consists of concatenated superconductive striplines that are held together via phenolic resin (AZ1350B photoresist) spun onto the Nb-coated silicon wafers. After the sandwich is created, the striplines are connected with wire bonds at the associated interfaces.

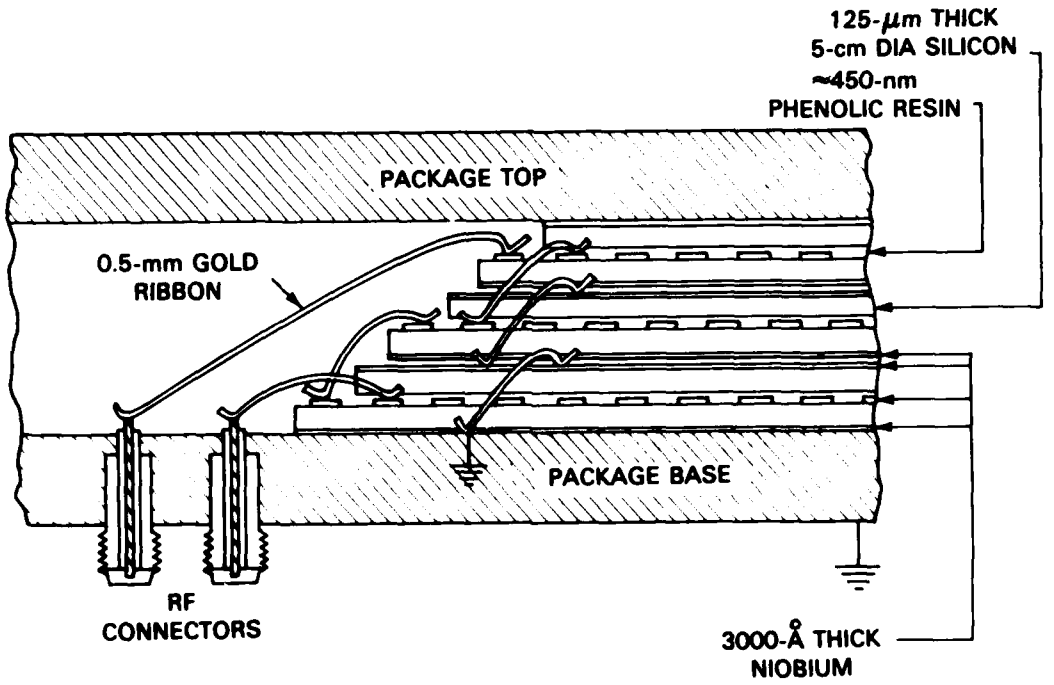

Figure 5-7. Stacked superconductive delay lines.

We have fabricated chirp filters with a two-wafer-pair configuration that have a 2.6-GHz bandwidth and a 75-ns dispersion time in addition to a three-wafer-pair structure with the same bandwidth and a 112-ns dispersion time. Using two matched 75-ns chirp filters, one with a Hamming weighting function and the other with a flat weighting, we have produced a compressed pulse with side lobes at -23 dB relative to the main lobe (Figure 5-8).

The phenolic resin shown in Figure 5-7 is a constituent of the composite dielectric in the stripline structure. In order to determine the electrical characteristics of this composite dielectric, a diagnostic stripline resonator was constructed using a thin layer of phenolic resin between the two silicon substrates. The presence of a 375-nm film of AZ1350B (0.15% of the total dielectric thickness) was found to increase the effective loss tangent of the composite dielectric by less than 2×10^{-5}. Doubling the thickness of this interfacial layer leads to an approximate doubling of this added loss tangent. The resonant frequencies of the resonator fabricated with this phenolic resin were repeatable to within approximately one part in 10,000 after each of five thermal cycles between room temperature and liquid-helium temperature. This stability is a factor of six better than that achieved with the same device without the resin but with the wafers clamped together by an array of BeCu springs (as is used for all non-resin-coated devices). The technique therefore offers improvement for even single-wafer-pair structures.[8]

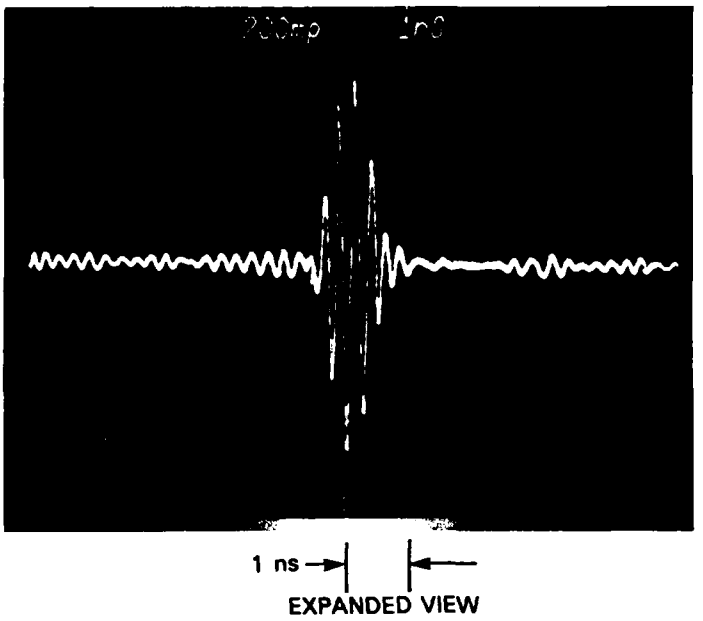

Figure 5-8. Compressed pulse response of matched stacked superconductive dispersive delay lines.

The mechanical stability, adequately low loss, and extended delay times of such stacked superconductive dispersive delay lines are consistent with requirements for lines with 500-ns delay and TB products greater than 1000. They therefore hold promise for use in high-performance analog-signal-processing systems.

J.B. Green

5.3 ADAPTIVE CANCELLATION OF SLOWLY VARYING RESPONSES OF LINEAR TIME-VARYING SYSTEMS

A technique has been developed for the adaptive cancellation of the slowly varying portion of the response from a time-varying system. Unlike conventional techniques that require repeated identical inputs, this technique allows the system to be interrogated using a wide-bandwidth non-repeating noise-like signal.

In acoustic or electromagnetic scattering measurements it is often necessary to probe the impulse response of a linear system and separate the uninteresting slowly varying or fixed portion of the response from the more interesting rapidly changing features. This is most often done by driving the system with some type of repeated signal and then subtracting the subsequent outputs of the system. Since the inputs do not change, the outputs due the fixed portion of the system's impulse response will cancel.

The signal used to probe the system's response must have certain properties. It must have sufficient bandwidth to resolve the details of the system's impulse response, and it must also contain sufficient energy so that the output signal may be detected with an adequate signal-to-noise ratio. Although a short pulse has the required bandwidth, in practice it is difficult to generate short pulses with large amounts of total energy since such pulses are often peak-power limited. In practice, wide-bandwidth phase-modulated signals are often used, and the system's output is then matched filtered against a time-reversed reference. This results in an output equal to the ideal output convolved with the autocorrelation function of the signal used.

In many applications it is advantageous to use random noise-like signals to probe the system instead of repeated deterministic signals. In this case, subtracting the outputs corresponding to subsequent inputs will not result in the cancellation of the fixed response from the system because the input signals will have changed. In order to obtain cancellation of the fixed portion of the system's response while the input signals change, it is necessary to develop a technique which separates the information of the system's response from the properties of the input signal. This can be done by using the output signals to generate an estimate of the fixed portion of the system's impulse response. This estimate of the impulse response can then be convolved with the subsequent input signal to generate an estimate of the subsequent output signal. By subtracting the estimated output from the actual output, one is left with the response due to the changing portion of the impulse response together with the residue due to errors in the estimates. This residue can then be used as an error signal to correct the previous estimate of the fixed impulse response.

Figure 5-9 depicts the architecture of such a canceler. First, a signal $s_n(t)$ is input into the linear time-varying system of interest. An estimate of the system's impulse response is simultaneously convolved with this input signal to form an estimate of the system's output. The convolution is performed by programming a transversal filter with weights corresponding to the estimated response $\hat{c}_n(t)$ of the system and driving the programmable transversal filter with the same

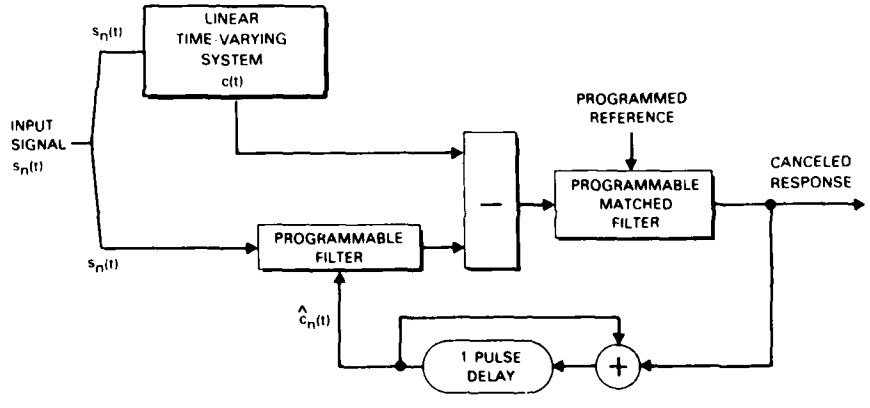

146144-N-04

Figure 5-9. Architecture of the adaptive canceler. The closed-loop design results in short convergence time and better accuracy in cancellation.

signal as was input to the system. Therefore, the transversal filter is essentially a model of the real system. The canceled output is formed by subtracting the output of the programmable filter from that of the real system and is then passed through a programmable matched filter that has been programmed with the time-reversed input signal as its impulse response. The output of the matched filter then contains the rapidly varying portion of the system's output.

This of course assumes that a good estimate of the system's response has already been formed. The function of the remainder of the adaptive canceler is to form an accurate estimate, $\hat{c}_n(t)$, of the system's impulse response c(t). If the estimate of the impulse response is not perfect, the output of the matched filter will contain an error signal corresponding to the difference between the actual impulse response of the system and the estimated impulse response of the system. However, this error signal will be corrupted due to the autocorrelation side lobes generated in the matched filtering process. The effects of these side lobes can be minimized and the rapidly changing portion of the system's response removed by integrating together all the matched filter outputs. This is done by using a recirculating delay line and an accumulator. The length of the delay line is equal to the time between input signals to the system. The output of the integrator is then used to program the response of the transversal filter.

The performance of such a canceler has been analyzed to determine the cancellation as a function of the rate of change of the impulse response, the convergence rate of the loop, and the correlation side lobes.

In order to quantify the performance of the canceler, a measure of the rate of change of the system's impulse response is needed. The frequency spectrum of these changes can be determined by finding the impulse response at regular intervals in time, in particular the interval between the generation of input signals, and calculating the discrete Fourier transform (DFT) across this set of impulse responses for a fixed time delay from the beginning of the intervals. High frequencies then correspond to rapidly changing components of the impulse response and low frequencies to the slowly varying components. The response of the canceler as a function of frequency, R(f), can be shown to be

$$R(f) = \left| \frac{1 - e^{2\pi jfT}}{1 - (1 - \mu)\, e^{2\pi jfT}} \right|$$

where μ is the gain of the adaptive loop ($0 \leq \mu \leq 1$), f is the frequency of change of the impulse response, and T is the period at which the system's impulse response is measured. A plot of cancellation as a function of the frequency of change of the system's impulse response is shown in Figure 5-10.

Analysis also shows that the canceler converges at a rate of 3 dB per pulse. This means that in 14 pulses the canceler can converge within 1% of total nulling from a starting state of no cancellation. In addition, the analysis shows that performance degradation due to correlation side lobes can be expressed as a fixed multiplicative loss in cancellation of the order of 1 dB.

A brassboard implementation of this technique is under construction. SAW/FET devices[9] will be used to provide the programmable transversal filtering function.

C.A. Bouman

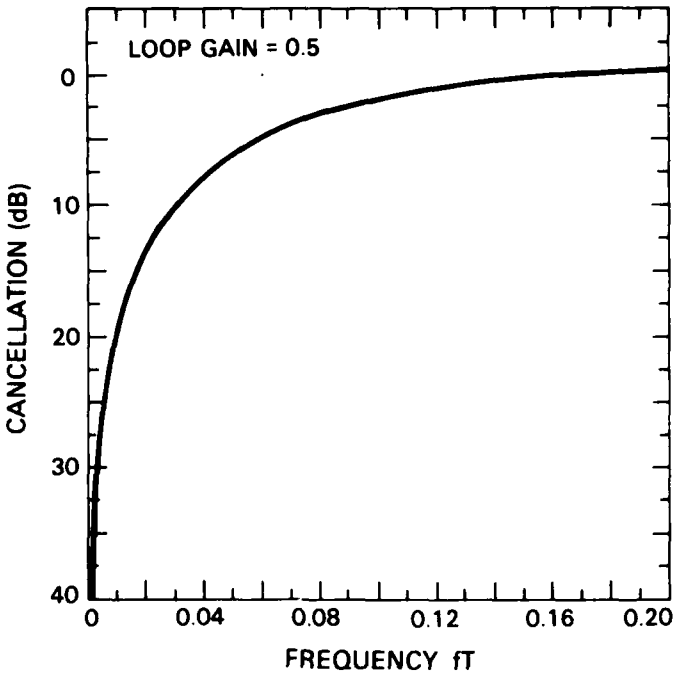

146147-N-01

Figure 5-10. The response of the canceler vs. the frequency of change of the system's impulse response. T is the interval between input signals.

REFERENCES

1. M. Nisenoff and E.A. Edelsack, in *Refrigeration for Cryogenic Sensors*, NASA Conf. Pub 2287, p. 1 (1982).
2. Solid State Research Report, Lincoln Laboratory, M.I.T., (1982:3), p. 74, DTIC AD-A124305.
3. T. Van Duzer and C.W. Turner, *Principles of Superconductive Devices and Circuits* (Elsevier, NY, 1981).
4. D.C. Mattis and J. Bardeen, Phys Rev **111**, 412 (1958).
5. S.R. Stein and J.P. Turneaure, in *Future Trends in Superconductive Electronics*, B.S. Deaver, Jr., C.M. Falco, J.H. Harris, and S.A. Wolf, eds., American Institute of Physics Conference No. **44**, 192 (1978).
6. Films provided by A.I. Braginski, Westinghouse Research & Development Center, Pittsburgh, PA.
7. Films provided by E. Cukauskas, Naval Research Laboratory, Washington, DC.
8. R.S. Withers, A.C. Anderson, J.B. Green, and S.A. Reible, IEEE Trans. Magnetics **MAG-21**, 186 (1985).
9. Solid State Research Report, Lincoln Laboratory, M.I.T., (1984:3), p. 75, DTIC AD-A154783.

☆ U.S. GOVERNMENT PRINTING OFFICE: 1985-600-000/20013

REPORT DOCUMENTATION PAGE		READ INSTRUCTIONS BEFORE COMPLETING FORM
1. REPORT NUMBER ESD-TR-85-214	2. GOVT ACCESSION NO.	3. RECIPIENT'S CATALOG NUMBER
4. TITLE *(and Subtitle)* Solid State Research		5. TYPE OF REPORT & PERIOD COVERED Quarterly Technical Report 1 February — 30 April 1985
		6. PERFORMING ORG. REPORT NUMBER 1985:2
7. AUTHOR*(s)* Alan L. McWhorter		8. CONTRACT OR GRANT NUMBER*(s)* F19628-85-C-0002
9. PERFORMING ORGANIZATION NAME AND ADDRESS Lincoln Laboratory, M.I.T. P.O. Box 73 Lexington, MA 02173-0073		10. PROGRAM ELEMENT, PROJECT, TASK AREA & WORK UNIT NUMBERS Program Element No.63250F Project No.649L
11. CONTROLLING OFFICE NAME AND ADDRESS Air Force Systems Command, USAF Andrews AFB Washington, DC 20334		12. REPORT DATE 15 May 1985
		13. NUMBER OF PAGES 74
14. MONITORING AGENCY NAME & ADDRESS *(if different from Controlling Office)* Electronic Systems Division Hanscom AFB, MA 01731		15. SECURITY CLASS. *(of this Report)* Unclassified
		15a. DECLASSIFICATION DOWNGRADING SCHEDULE

16. DISTRIBUTION STATEMENT *(of this Report)*

Approved for public release; distribution unlimited

17. DISTRIBUTION STATEMENT *(of the abstract entered in Block 20, if different from Report)*

18. SUPPLEMENTARY NOTES

None

19. KEY WORDS *(Continue on reverse side if necessary and identify by block number)*

solid state devices	photodiode devices	infrared imaging
quantum electronics	lasers	surface-wave transducers
materials research	laser spectroscopy	charge-coupled devices
microelectronics	imaging arrays	acoustoelectric devices
analog device technology	signal processing	

20. ABSTRACT *(Continue on reverse side if necessary and identify by block number)*

This report covers in detail the solid state research work of the Solid State Divison at Lincoln Laboratory for the period 1 February — 30 April 1985. The topics covered are Solid State Device Research, Quantum Electronics, Materials Research, Microelectronics, and Analog Device Technology. Funding is primarily provided by the Air Force, with additional support provided by the Army, DARPA, Navy, NASA, and DOE.

DTIC

END

4-86